THE JOURNAL OF PHYSICAL CHEMISTRY C

Article

Low Valence Cation Doping of Bulk CrO: Charge Compensation and Oxygen Vacancy Formation

John J J Carey, Merid Legesse, and Michael Nolan

J. Phys. Chem. C, **Just Accepted Manuscript** • DOI: 10.1021/acs.jpcc.6b05575 • Publication Date (Web): 09 Aug 2016

ACS Publications

The Journal of Physical Chemistry C is published by the American Chemical Society. 1155 Sixteenth Street N.W., Washington, DC 20036

Low Valence Cation Doping of Bulk Cr_2O_3: Charge Compensation and Oxygen Vacancy Formation

John. J. Carey, [a*] Merid Legesse,[b] and Michael Nolan [a]*

[a] Tyndall National Institute, University College Cork, Lee Maltings, Prospect Row, Cork, Ireland

[b]Qatar Environment and Energy Research Institute, Hamad Bin Khalifa University, Qatar Foundation, Doha, Qatar

ABSTRACT: The different oxidation states of chromium allow its bulk oxide form to be reducible, facilitating the oxygen vacancy formation process, which is a key property in applications such as catalysis. Similar to other useful oxides such as TiO_2, and CeO_2, the effect of substitutional metal dopants in bulk Cr_2O_3 and its effect on the electronic structure and oxygen vacancy formation are of interest, particularly in enhancing the latter. In this paper, density functional theory (DFT) calculations with a Hubbard +U correction (DFT+U) applied to the Cr 3d and O 2p states, are carried out on pure and metal doped bulk Cr_2O_3 to examine the effect of doping on the electronic and geometric structure. The role of dopants in enhancing the reducibility of Cr_2O_3 is examined to promote oxygen vacancy formation. The dopants are Mg, Cu, Ni, and Zn, which have a formal +2 oxidation state in their bulk oxides. Given this difference in host and dopant oxidation states, we show that to predict the correct ground state two metal dopants charge compensated with an oxygen vacancy are required. The second oxygen atom removed is termed 'the active' oxygen vacancy and it is the energy required to remove this atom that is related to the reduction process. In all cases, we find that substitutional doping improves the oxygen vacancy formation of bulk Cr_2O_3 by lowering the energy cost.

1. Introduction

Chromium forms different metal oxides, including α-Cr_2O_3 (corundum structured), CrO_2 (rutile structured), and Cr_5O_{12} (with unconnected strings of CrO_4). The only stable bulk oxide is α-Cr_2O_3, which is an antiferromagnetic dielectric in which the oxygen atoms form a hexagonal closed packed array. The chromium cations occupy two thirds of the octahedral interstices between the two layers.[1] The primitive cell can be described as a rhombohedral structure with the chromium atoms being six coordinated and the oxygen atoms being four coordinated in oxygen layers above and below the chromium layer. α-Cr_2O_3 is a wide band-gap semi-conductor with an experimentally measured direct band-gap of 3.3eV.[2,3] Density functional theory calculations (DFT) using the generalized gradient approximation (DFT-GGA), underestimate the band gap, giving band gaps in the range of 2.8-3.1eV.[4-6] When using a screened-exchange hybrid functional a band gap of 3.31eV is obtained.[7] Regarding the magnetic properties of Chromia the ground state is anti-ferromagnetic (AFM) with possible magnetic orderings in the Cr-containing layers of "--++", "-+-+" and "-++-" where '+' and '-`denote the quantum spin α and β states, respectively. Previous work has shown that the "-+-+" spin ordering correctly describes the ground state structure for α-Cr_2O_3, in a similar fashion to Fe_2O_3.[5-8], The electronic structure of α-Cr_2O_3 is borderline between charge transfer and Mott-Hubbard insulator, because the Cr 3*d* states mix with O 2*p* states at both the valence band maximum (VBM) and conduction band minimum (CBM). This orbital mixing in the VBM and CBM is supported by photoemission and electron-energy-loss spectroscopy,[9] and X-ray photoemission spectroscopy.[10]

Conundrum structured α-Cr_2O_3 has attracted much interest for its potential use in a wide range of applications, including catalysis,[11-15] as an anode material in Li-ion batteries,[16] in gas sensors,[17] solid oxide fuel cells,[15] protective coatings[18,19] and adhesion promotors.[20] To improve the performance of Cr_2O_3 for

more efficient utilization in many of these applications, a key property is that of oxygen vacancy formation, which is important in redox reactions and for lattice oxygen mobility.

Oxygen vacancy formation in a metal oxide can be enhanced by introducing substitutional dopants on the cation site. This has been extensively explored for the reducible metal oxides TiO_2[21-24] and CeO_2[25-28] from both experiment and theory. The introduction of a substitutional dopant on the host cation site alters the electronic and local geometric structure of the host and this can promote the formation of oxygen vacancies and migration of oxygen. Substitutional dopants, which have a lower oxidation state in their parent oxide compared to the oxidation state of the cation in the host oxide (lower valence dopants, LV) create an effective positive charge at the anion lattice position. This is the well-known oxygen hole. In contrast, dopants that have a higher oxidation state in their parent oxide than that of the cation in the host oxide (higher valence dopants, HV), have effective negative charges at the cation lattice site, giving localization of excess electrons at a host cation.

Early Mott-Littleton calculations by Catlow *et al.*[29] studied intrinsic defects in the bulk structures of α-Fe_2O_3 and α-Cr_2O_3. The defect formation energies and diffusion barriers in bulk α-Cr_2O_3 indicated that the reduction energies for oxygen vacancy formation and Cr cation diffusion were relatively low, suggesting that the material possesses good redox properties. Nitrogen doped Cr_2O_3 has received a high degree of attention for applications in optoelectronic devices as the presence of N increases the hole mobility in the material. The N atom substitutionally replaces an O atom, and with one less electron, this can make a suitable hole transporting layer for organic solar cells.[30-33] Doping of Cr_2O_3 with Mg has been documented to change the electronic structure to induce *p*-type semiconductor behavior by creating a hole that arises from replacing a Cr^{3+} cation with an Mg^{2+} dopant [34-39] however, the optical properties eventually degrade over time, thus making the material inactive. To improve the optical and electronic properties of $Cr_2O_3$and overcome the issues associated with Mg: Cr_2O_3, co-doping with Mg and N was examined.[36,40,41] Nitrogen doping was found to improve the transmission properties and electronic

conductivity of Cr_2O_3 through band gap widening and the presence of NO_3^- in the system; Mg doped Cr_2O_3 showed no enhancement of these features over the undoped Cr_2O_3 lattice, but probably acts to stabilize the N-doping. A recent combined experimental and DFT study using the PBE-GGA approach with Hubbard + U correction (PBE+U) investigated Mg doping of Cr_2O_3 under different growth conditions of Cr-rich/O-poor, O-rich/Cr-poor. The results show that in the O-rich regime an Mg dopant on a Cr cation site is uncompensated, and displays *p*-type conductivity under optimal growth conditions.[42] No conductivity is found under O-poor conditions, where Mg is likely to be compensated. Experimental XPS/XRD and DFT (LDA+U) investigations of N-F co-doping of Cr_2O_3 showed that the structure was greatly distorted by the presence of N atoms, which were charge compensated by the F dopants[43] This reduced the d-d band gap by 0.6 eV, and changed the character to p-d. Doping also altered the magnetic structure and optical properties of Cr_2O_3 through hole-mediated exchange and spin-orbit coupling, thus improving its capabilities for applications in spintronic and optoelectronics applications. Ca and Ti doping of Cr_2O_3 have been examined with DFT (PW91+U), which showed that the inclusion of the dopants can reduce the fundamental band gap by up to 0.4eV for Ca doping, but with no change in the fundamental band gap for Ti doped Cr_2O_3. For the doping of Cr_2O_3 with Ca, there are no defect levels observed in the band gap as Ca states lie low in the VB (~-20eV) and high in the CB (~+10eV), while for Ti a β-spin peak is shown to occur in the band gap which is attributed to the Ti impurity; however it is not mentioned if this electron is localized on the Ti atom or reduces a neighboring Cr cation.[5,8] As the Ca^{2+} dopant replaces lattice Cr^{3+} cation, a hole is expected to form on a neighboring oxygen atom as Ca^{2+} replaces Cr^{3+} and located at the VB edge, perhaps pushing the VB to a higher energy; however this is not mentioned and no charge compensation mechanism is discussed. Fe doped Cr_2O_3 was investigated with Fe having a 3+ oxidation state.[44] The larger ionic radius of Fe^{3+} resulted in expansion of the cell volume (ionic radii: Fe^{3+} ~0.67Å and Cr^{3+} ~0.61Å).[44] An optical band gap in the range of 3.09eV to 3.44eV was determined from a Tauc plot for different concentrations of Fe dopant (0-4 wt%). Further-

more, Fe doping resulted in an increase in the concentration of charge carriers and this was attributed to Cr vacancy formation.

The studies described above outline some effects arising from dopant incorporation into the Cr_2O_3 lattice, and the resulting modifications to the electronic structure. However apart from Mg-Cr_2O_3,[42] the effect of a dopant on the oxygen vacancy formation in Cr_2O_3, which is a key property for applications in fuel cells, solar cells and catalysis, has not been examined in any detail in the previous literature, in particular when compared to other reducible metal oxides such as TiO_2 and CeO_2.

Early theoretical and experimental studies indicated that anion diffusion is slower than cation diffusion in Cr_2O_3.[29,45] More recent studies have however indicated that oxygen diffusion is more facile, in particular along grain boundaries, thus indicating that structural defects as well as doping in Cr_2O_3 can improve its oxygen mobility.[46-48]

The introduction of holes through incorporating a LV dopant will lead to spontaneous formation of oxygen vacancies to compensate the lower oxidation state of the dopant compared to the host.[49-52] The resulting absence of oxygen in the lattice after the release of oxygen can be experimentally observed, as the vacancy cannot be annealed in the presence of oxygen. Given that this vacancy will therefore always be present, it will induce structural distortions, which can lead to potentially more favorable oxygen vacancy formation and mobility. To maintain charge neutrality, and give the correct ground state electronic structure after incorporation of the dopant, neutral oxygen vacancies release electrons to fill the holes formed from incorporation of the LV dopant. The formation of charge compensating oxygen vacancies can be described in the following reactions, using Kröger-Vink notation for a lower valent metal (M) dopant in Cr_2O_3;

$$Cr_{Cr}^{x} + O_o^x + M_2O \rightarrow M_{Cr}'' + 2O_O^{\cdot} + Cr_2O_3 \qquad (1)\ \text{(Oxygen Hole Formation)}$$

$$M_{Cr}'' + 2O_O^{\cdot} + O_o^x \rightarrow M_{Cr}'' + 2O_O^x + V_o^{\cdot\cdot} \qquad (2)\ \text{(Oxygen Hole Compensation)}$$

where Cr_{Cr}^{x} is a neutral Cr cation on a Cr^{3+} lattice site, M is a metal dopant that has an oxidation state of +1, $M_{Cr}^{\prime\prime}$ is the metal substituting a Cr^{3+} lattice site with an effective charge of -2, $2O_{\dot{O}}$ is a hole on an oxygen lattice site forming O^{-} (polaron), and $V_{\ddot{O}}$ is the formation of an oxygen vacancy at an O^{2-} lattice site with an effective charge of +2 that acts as a charge compensating species. In equation (1), a substitutional LV metal dopant with a +1 oxidation state on a Cr^{3+} site induces holes (O^{-} species) on two oxygen species. This is compensated by an oxygen vacancy that releases two electrons to compensate the holes, equation (2). This is critical to correctly describe the ground state electronic structure for modelling and investigating LV dopants in a metal oxide, [53-56] If the system is not charge compensated the material is not charge neutral which can lead to issues in calculating properties such as over-binding of electron rich adsorbates.

In the present paper, we apply DFT, with a Hubbard +U correction (PBE+U) to examine the incorporation of dopants with a formal +2 oxidation state in their native oxides, namely Mg, Ni, Cu and Zn onto Cr^{3+} lattice sites in bulk Cr_2O_3. In this case, to correctly describe and charge balance dopants with a +2 oxidation state,[39] that produce a hole on one neighboring lattice oxygen, two metal dopants on Cr sites are compensated by an oxygen vacancy as follows;

$$2Cr_{Cr}^{x} + O_{o}^{x} + \mathrm{M}O \rightarrow 2M_{Cr}^{\prime} + V_{\ddot{O}} + 2Cr_2O_3 \qquad (3)$$

We have presented a similar study of LV dopants, Al^{3+}, Ga^{3+} and In^{3+} in bulk rutile TiO_2,[49] where charge compensated structures were studied. We also found that while PBE+U gives positive, albeit small, formation energies for the compensating oxygen vacancy, using the Heyd–Scuseria–Ernzerhof (HSE) screened hybrid DFT functional[57] showed that the first oxygen atom forms spontaneously with a negative formation energy. The active oxygen vacancy, that is the vacancy of interest in an oxidation reaction, is the second oxygen atom and the energy cost associated with the removal of this atom is the oxygen vacancy formation energy we use to assess the reducibility of the material. Similar studies have been presented for doped CeO_2, [51,55,56,58,59] and confirm the importance of including charge compensat-

ing vacancies to correctly describe the ground state electronic structure of doped metal oxides. Previous DFT studies on doping of Cr_2O_3 have neglected the need for a charge compensating mechanism and this can lead to questionable results.[5] A key contribution of this paper is to present in detail the effect of LV doping in Cr_2O_3, with the inclusion of charge compensation, to correctly describe enhanced oxygen vacancy formation energies that may result in improved catalytic performance of Cr_2O_3.

2. Computational Methods:

All calculations have been performed using DFT employed in the Vienna *Ab initio* Simulation Package (VASP).[60-62] The generalized gradient approximation (GGA) method[63] was used with the Perdew-Burk-Ernzerhof (PBE) exchange-correlation functional.[64] The valence states were expanded in terms of a plane wave basis set[65] and the electron-ion interactions were described by the projected augmented wave (PAW) method.[66] The core and valence electron configurations are, Cr[Ar] d^5 s^1, O[He] s^2 p^4, Mg[Be] p^6 s^2, Ni[Ar] s^2 p^6 d^8 , Cu[Ar] d^{10} p^1, and Zn[Ar] d^{10} p^2.

The Brillouin zone integrations were sampled using the Monkhorst-Pack method,[67] and *k*-point sampling grids of 2x2x2, 4x4x4 and 6x6x6 were tested on the bulk Cr_2O_3 corundum structure at a 500eV plane wave cut-off. The structural optimizations of the Cr_2O_3 bulk were carried out using a conjugate-gradient algorithm, and performed at a series of volumes where the atomic positions, forces and cell angles were allowed to relax while keeping the cell volume constant. The resultant energies were fitted to the Murnaghan equation of state[68] to obtain the minimum energy structure. The minimum energy structure was obtained using a *k*-point sampling grid of 4x4x4 at a 500eV energy cut-off with a lattice parameter of $a=b=5.08$Å and $c=13.99$Å, which deviates from the experimental structure by 2.48%.[69] This optimized unit cell was expanded to a (2x2x2) supercell, with composition $Cr_{96}O_{144}$ and relaxed using a similar plane wave cut off energy with a 2x2x2 *k*-point sampling grid to keep a consistent *k*-point density. This supercell is used to investigate oxygen vacancy formation in undoped bulk Cr_2O_3, and for all

doped structures; this results in a doping concentration of 1.04% for single dopants and 2.08% with two dopants.

To correct for the strong electronic correlation within bulk Cr_2O_3, the DFT+*U* method in the form proposed by Liechtenstein[70] and Dudarev *et al.*[71,72] and implemented in a PAW approach by Bengone *et al.*[73] were used in this study. The implementation of GGA+*U* within the VASP code combines the Hubbard-like description of the on-site correlations with spin polarised DFT calculations.[74] As the Cr_2O_3 bulk is known to be anti-ferromagnetic, the on-site potential +*U* correction is necessary to describe the correct ground state electronic and magnetic structure of Chromia. A range of U values, that is from U = 1 eV to U = 8 eV on the Cr 3d states, were previously studied for bulk Cr_2O_3 and the effect of the +U correction on the cell volume and the magnetic and electronic structures was studied, making comparison to available experimental data.[6] A value of *U* of 5 eV was found to deliver a reasonable compromise between calculations and experiment and we therefore use this value of U for all calculations in this study. We note however, that the application of the DFT+U approach has not been examined oxygen vacancy formation in bulk chromia, but extensive studies on transition metal oxides and ceria have shown that the DFT+U approach describes the oxygen vacancy formation process very well. In this paper we are interested in how the bulk oxygen vacancy formation energy is affected by substitutional doping on the Cr site and it is the trends with doping that are important and these will be well described by the present DFT+U set-up.

The introduction of a lower valent metal dopant on the Cr cation site creates holes on neighboring oxygen atoms, since the LV dopant has fewer electrons than the Cr cation. It is now well known that these states cannot be described by the standard approximate DFT LDA and GGA exchange-correlational functional and will be delocalized across multiple oxygen atoms, which is physically unrealistic. To correctly localize the hole states on one oxygen atom, a +*U* correction of 5.5eV is applied to the O 2*p* states in all calculations. This has been widely discussed in previous studies for doping of CeO_2 and

TiO_2.[58,59,75] The magnetic structure of Cr_2O_3 is difficult to correctly model, requiring a DFT+U level or better, and previous work found that a magnetic ordering of alternating + and – layers within the bulk along the *c*-axis accurately describes the ground state magnetic structure which is also used in this work.[4,7,14,76]

The electronic density of states (EDOS) was sampled at a higher *k*-point mesh using a 8x8x8 grid with a Gaussian smearing approach and a broadening of σ=0.1eV was used. Partial (ion and *l*-quantum number decomposed) electronic density of states (PEDOS) were calculated by projecting the electronic eigenstates onto their spherical harmonic components as described by PAW radii, which allow a detailed analysis of the electronic structure.

The oxygen vacancy formation energy (E[Ovac]) for bulk Cr_2O_3 was calculated by;

$$E[Ovac] = E(Cr_2O_{(3-x)}) + ½\ E(O_2) – E(Cr_2O_3) \quad (4)$$

Where $E(Cr_2O_{3-x})$ is the energy of bulk Chromia (doped or undoped) with an oxygen vacancy, $E(O_2)$ is the calculated energy of gaseous O_2 and $E(Cr_2O_3)$ is the calculated energy for pure bulk Cr_2O_3. The Hubbard +U value of 5.5eV applied to the O 2p states of molecular O_2 can correct for the known over binding of standard PBE.

Oxygen vacancy formation is examined for two cases. The first is the uncompensated $[M'_{Cr} + V_{\ddot{O}}]$ defect in the lattice with one dopant and the oxygen vacancy fills the hole state, partially reducing two neighboring Cr^{3+} cations to two $Cr^{(3-\delta)+}$ species (See Secion 3.2). A second metal dopant is introduced onto a Cr site to model the $[2M'_{Cr} + V_{\ddot{O}}]$ defect, for which the compensating oxygen vacancy is examined. Here we will also compare PBE+U and HSE in describing this process. For the HSE approach, a screening length of 20% Hartree-Fock exchange is implemented. The removal of the next oxygen species, which is termed the active oxygen vacancy, is examined and we compare which metal species gives the most favorable oxygen vacancy formation energy.

The formation energy for the charge compensating oxygen vacancy is calculated by;

$$E[Ocomp] = E(M_x:Cr_{(2-x)}O_{(3-x)}) + \tfrac{1}{2}\, E(O_2) - E(M_x:Cr_{(2-x)}O_3) \qquad (5)$$

where $E(M_x:Cr_{(2-x)}O_{(3-x)})$ is the energy for the M doped Cr_2O_3 lattice with the compensating oxygen vacancy, and $E(M_x:Cr_{(2-x)}O_3)$ is the energy for the M doped Cr_2O_3 lattice. The number of metal atoms can vary depending on the oxidation state of the dopant, but the formula remains consistent. The energy for the active oxygen vacancy is calculated in a similar manner with a second oxygen removed from $M_x:Cr_{(2-x)}O_{(3-x)}$ system, and the compensated structure is used as the reference.

3. **Results**:

3.1 Bulk and reduced α-Cr_2O_3

The calculated atomic structure for a unit cell of bulk α-Cr_2O_3 is shown in Figure 1 (a); the Cr^{3+} cations and O^{2-} anions are indicated by the blue and red spheres throughout this paper. Chromium cations adopt a six-coordinate octahedral geometry while the oxygen anions possess a four coordinate tetrahedral geometry within the Cr_4O_6 layers. The octahedral geometry for the Cr^{3+} cations is shown in Figure 1(b) with the six oxygen neighbors labelled and the corresponding Cr-O bond distances are given in Table 1.

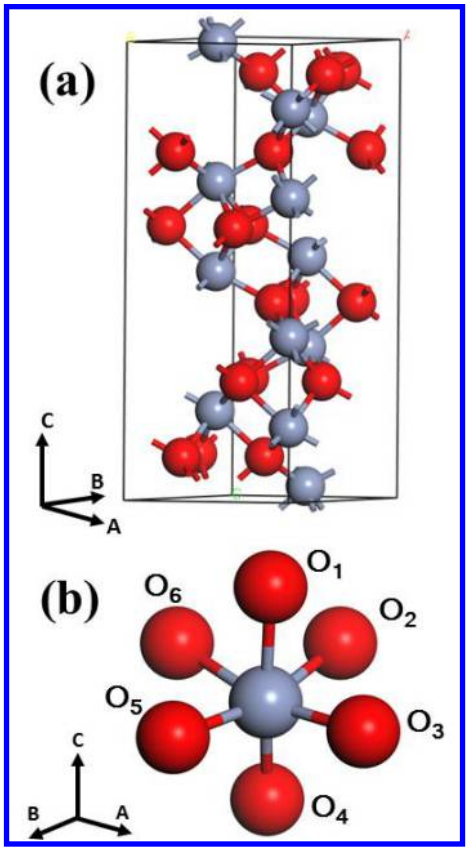

Figure 1: The atomic structure (a) and local cation geometry (b), for bulk α-Cr_2O_3. The blue and red spheres represent the lattice positions for Cr and O respectively. The orientation along the *a*-, *b*- and *c*-vectors is included to show the relative position of the cation geometry to the bulk unit cell.

Table 1: Calculated Cr-O bond distance (Å) for the Cr^{3+} cations in bulk α-Cr_2O_3

$Cr - O_x$ Bond	Calculated distance (Å)
$Cr - O_1$	2.05
$Cr - O_2$	2.05
$Cr - O_3$	2.02
$Cr - O_4$	2.02
$Cr - O_5$	2.02
$Cr - O_6$	2.05

To characterize the valence band (VB) and conduction band (CB) of bulk Cr_2O_3, the PEDOS was calculated and is shown in Figure 2. The PEDOS shows the interaction between the Cr 3d (blue) and O 2p (red) states that are primarily involved in bonding. The VB and CB originate from a mixing of these states with a calculated band gap of 2.66eV which is underestimated compared to the experimental band gap. This is typical for PBE+U calculations, where U is not set to reproduce the band gap, but is instead set to consistently describe charge localization, magnetic structure, and spin states that are sensitive to the selected +U value.[6,74] Recent DFT (PBE+U) calculations have fitted the band gap to experimental XPS data, obtaining a calculated fundamental indirect band gap of 2.96 eV with a +U correction of 3 eV and 5 eV applied to the Cr 3d states and O 2p states, respectively.[42] Our calculated value is only 0.3eV lower than this, indicating that our calculated band gap is within an acceptable difference.

The VB region shows strong mixing between Cr 3d and O 2p states, while the bottom of the CB shows larger contributions from the Cr 3d states than the O 2p states. The dominance of Cr 3d states at the VBM and CBM is indicative of a Mott insulator.[77] The contribution from the O 2p states at the top of the VB however, reduces the probability of Cr 3d - 3d transitions, and weak transitions between O 2p

states and Cr 3d states can occur making it a weakly charge transfer (CT) material. The introduction of defect levels through substitutional doping will alter the mixing of states at the VBM or CBM which may assist in tailoring the band gap of the material to allow more efficient transitions between dopant states and the Cr 3d states.

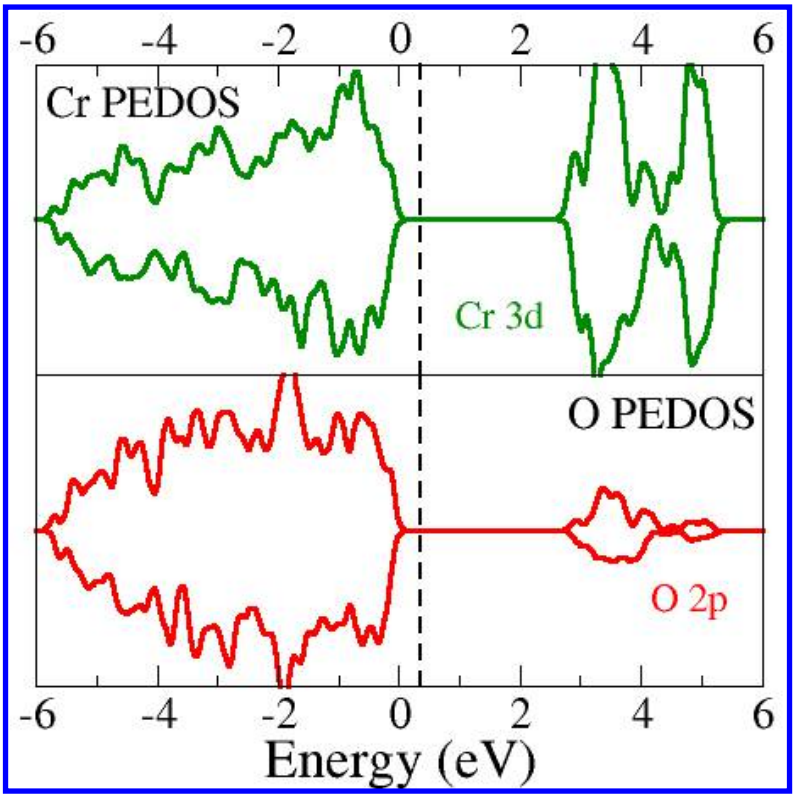

Figure 2: The calculated spin polarised PEDOS for bulk α-Cr_2O_3. The green and red lines are the Cr 3*d* and O 2*p* states, respectively. The top of the valence band is aligned to 0 eV and the dotted line indicates the calculated position of the Fermi Level.

Oxygen vacancy formation was investigated to serve as a benchmark for comparison of the oxygen vacancy formation energies with the doped systems. Since removal of an oxygen atom from its lattice position will affect only the local atomic structure around the vacancy, we show the local atomic structure around the vacancy in Figure 3(a); the location of the oxygen vacancy is shown by the black sphere in the figure. Examination of the local geometry around the oxygen vacancy indicates that the four near-

est neighbor Cr cations previously bonded to the oxygen atom are displaced from their lattice positions. They are found to move away from the vacancy site, and adopt a five coordinate square pyramidal geometry; the associated Cr-O bonds are shortened by a range of 0.2 – 0.4 Å.

Removal of a neutral oxygen species from its lattice site creates unpaired electrons that can reduce the neighboring, or next nearest neighboring cations, as in e.g. reduced CeO_2 or TiO_2. We have explored different Cr reduction sites and singlet or triplet ground state electronic configurations. Analysis of total energies, spin magnetization and Bader charge analysis shows that a singlet ground state electronic configuration is preferred. The singlet configuration is more stable than the corresponding triplet by up to 0.8eV, and after relaxation there are four partially reduced Cr cations, which we indicate as $Cr^{(3-\delta)+}$ since none of these sites are fully reduced to Cr^{2+}. To check the stability of partial reduction of the four Cr cations, structural distortions are induced by various approaches to localize the electrons to two neighboring Cr cations. However, these attempts result in relaxation back to the configuration presented in Figure 3. The locations of the partially reduced Cr sites are indicated by the orange Cr atoms in Figure 3(a) with the reduced Cr cations labelled 1 to 4. The singlet electronic configuration keeps the antiferromagnetic arrangement of Cr cations, with partially reduced Cr cations in the layer above the oxygen vacancy (Ovac) site having a different spin state to those in the layer below the Ovac.

The calculated PEDOS for reduced bulk Cr_2O_3 is shown in Figure 3(b). The reduction of the next nearest neighbor Cr cations from 3+ to (3-δ)+ is reflected in the presence of defect levels in the band gap of the reduced bulk as shown in the PEDOS. Cr 3d states become occupied from the reduction process with occupied defect peaks appearing at c.a. 0.7 eV and unoccupied peaks at 2.0eV above the top of the VB edge; this is shown for the reduced Cr cations in the bottom panel of the PEDOS plot. The spin up peaks are from Cr 1 and 2, as labeled in Figure 3(a), and the spin down contribution to the defect peaks is from the reduced Cr 3 and 4 atoms (Figure 3(a)) so that the system maintains its antiferromagnetic nature. The two peaks are spin paired due to the singlet ground state electronic configura-

tion from the four reduced Cr cations. The calculated oxygen vacancy formation energy for bulk α-Cr_2O_3 is 4.11eV.

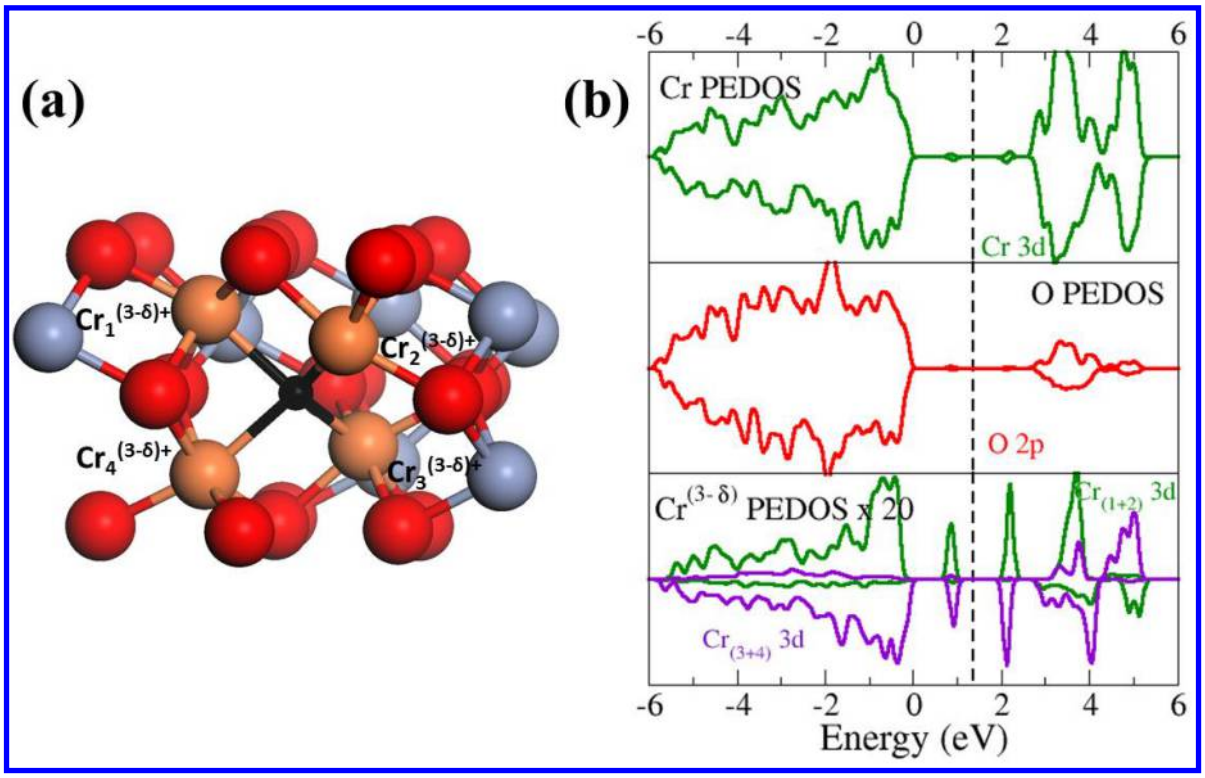

Figure 3: (a) The local atomic structure around the oxygen vacancy (indicated by a small black sphere) in bulk α-Cr_2O_3. The color coding is the same as figure 1 and the partially reduced Cr^{3+} cations are indicated by the orange spheres. (b) The calculated PEDOS for the reduced Cr_2O_3 bulk with the defect levels shown within the band gap. The top of the valence band is aligned to 0eV and the dotted line indicates the highest occupied state.

3.2 Substitutional doping of Lower Valence cations in bulk α-Cr2O3: hole and oxygen vacancy formation

We replace one Cr^{3+} cation in our supercell with a +2 metal dopant, giving a concentration of 1.04%. The presence of the dopant in the lattice distorts only the local geometry around the dopant and has no effect on the geometry beyond the next next nearest neighbor Cr cations. Only the calculated local geometry around the dopant is shown in Figure 4.

For Mg doped Cr_2O_3, Mg adopts a 5-fold square pyramidal geometry while Ni doping results in Ni maintaining the 6-fold octahedral geometry taken by the Cr^{3+} cations. Both Cu and Zn dopants adopt a 3-fold trigonal geometry, in which they bond to the three oxygens in the layer below while the oxygens in the layer above are now three-fold coordinated instead of four-fold coordinated in undoped Cr_2O_3. These coordination environments are typical of these metal dopants in metal oxide hosts.[50-52,78] Cu is not able to distort the corundum structure to allow a two-fold or four-fold coordination geometry, and is known to adopt a three-fold geometry in Fe_2O_3.[79]

The Mg-O distances range from 1.96Å to 2.15Å, and the Ni-O distances range from 1.99Å to 2.05Å; the latter are closer to typical Cr-O distances, indicating that Mg causes more distortions to the local atomic structure does Ni. The three Cu-O distances are 2.02Å and the three Zn-O distances are 1.99Å. These dopants have shorter metal-oxygen distances than Cr, Table 1. Therefore, the strongest distortions are induced by Cu and Zn doping onto Cr lattice sites.

The calculated PEDOS for each of the lowest energy configurations are shown in Figure 4. The Cr 3d states in the VB and CB appear to be relatively unaffected by the presence of the dopants in the lattice for all systems. For the O 2p states, an unoccupied peak corresponding to the oxygen hole state appears around 0.5eV above the top of the VB for Mg, Cu and Zn doped Cr_2O_3, while there are no hole states observed for the Ni doped bulk. The oxygen atom associated with the hole state is further identified by computed Bader charges that decrease from 7.3 (typical of O^{2-}) to 7.0 electrons, and a computed spin

magnetization of 0.5 electrons, consistent with an oxygen hole state. The location of the hole is shown in Figure 4 by the light blue sphere. The PEDOS for this oxygen is shown in the lower panel of the PEDOS plot for Mg, Cu and Zn doped Cr_2O_3 indicated by the "O hole PEDOS". The exception to this is Ni doped Cr_2O_3, in which Ni adopts a +3 oxidation state with no oxygen hole states present, confirmed by Bader analysis (oxygen charges of 7.3 electrons, and spin magnetization of 0), indicating that upon incorporation, Ni is isovalent to Cr^{3+}. Although this is a potentially surprising result as NiO is the stable oxide of Ni, previous work shows that Ni doped into Al_2O_3 and $LaAlO_3$ will take a +3 oxidation state,[80-83] suggesting that doping sesquoxides with Ni alters the dopant oxidation state to become isovalent with that of the host cation and we also note that the local geometry around Ni shows octahedral coordination, the same as Cr.

For Mg and Zn doped Cr_2O_3, the calculated Fermi levels are close to the top of the VB (Mg:0.0eV, Zn:0.2eV) with no metal dopant states appearing in the band gap. The fermi level is higher for Ni and Cu doped Cr_2O_3 being located at 0.4eV since these metals have 3d states above the Cr_2O_3 VB, which suggest that electron transfer is more facile in these systems than for the Mg and Zn doped lattices. Ni-Cr_2O_3 and Cu-Cr_2O_3 have 3d defect levels in the band gap above the Fermi Level which are not observed for Mg and Zn doping. For Cu-Cr_2O_3 there is an occupied Cu 3d peak just below the fermi level at 0.3eV above the top of the VB edge, while for Ni-Cr_2O_3 the occupied peaks are at the VB edge. The Cu dopant has a calculated Bader charge of 15.7 and a spin magnetization of 0.0 that is indicative of Cu^{2+} cations.

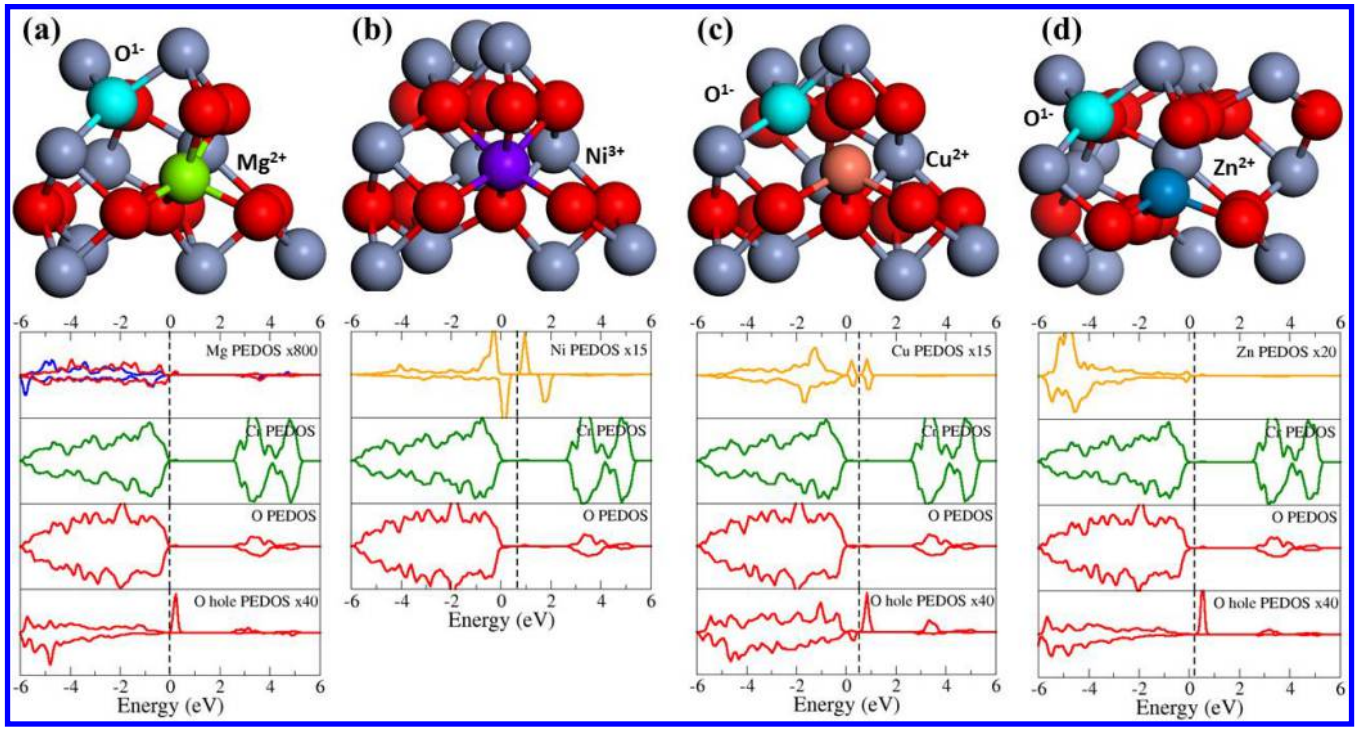

Figure 4: The local geometry and calculated PEDOS for (a) Mg, (b) Ni, (c) Cu, and (d) Ni doped α-Cr_2O_3. The grey and red spheres are the Cr^{3+} cations and O^{2-} anions, respectively, while the Mg, Ni, Cu and Zn dopants are the green, purple, orange and blues spheres. The blue, red, orange and green lines on the PEDOS plots are the *s*, p, dopant 3*d* and Cr 3*d* states with the top of the valence band aligned to 0eV and the dotted line shows the position of the Fermi level.

Oxygen vacancies are investigated for each dopant to examine the effect of the dopant on their formation energy, and the location of the electron released by the neutral vacancy. We examined the removal of all oxygen atoms surrounding the metal dopant, in the layers above and below the dopant to determine the lowest energy configuration (See supplementary information Tables S1 – S4 for the range of computed oxygen vacancy formation energies). The most stable oxygen vacancy sites are shown in Figure 5. The calculated energies for the lowest energy configuration of the oxygen vacancy formation in each of the doped systems are given in Table 2. In all cases doping greatly improves the oxygen va-

cancy formation energy in Cr_2O_3, with the Cu-Cr_2O_3 system having the lowest formation energy, suggesting it promotes more favorable vacancy formation over the other dopants. For all doped structures, the most favorable position of the oxygen vacancy is next neighbor to the dopant cation. This therefore reduces the coordination of the dopants in Cr_2O_3. The Mg and Ni dopants form four coordinated square planar configurations, which have been found in doping of other oxides[51,78], while Cu and Zn are now two-fold coordinated, in which they bridge with two neighboring oxygen atoms from the loss in coordination after oxygen vacancy formation. Cr cations neighboring the oxygen vacancy site also display reduced coordination – going from 6 fold octahedral coordination to a distorted 5 coordinated square pyramidal configuration.

Table 2: The calculated oxygen vacancy formation energies, relative to ½ O_2, for undoped and doped Cr_2O_3

	E[Ovac] (eV)
Undoped Cr_2O_3	4.11
Mg-Cr_2O_3	2.53
Ni-Cr_2O_3	2.45
Cu-Cr_2O_3	1.87
Zn-Cr_2O_3	2.86

The formation of an oxygen vacancy releases two electrons into the system. One of these electrons fills the hole on the neighboring oxygen species and the other electron reduces neighboring Cr^{3+}. The reduced Cr species are indicated by the orange spheres in Figure 5. This is confirmed by the computed Bader charges and the spin magnetizations. The Bader charge on the oxygen carrying the hole increases from 7.0 to 7.3 electrons, indicating filling of the hole. For Mg and Cu, there are two partially reduced Cr cations, each with a Bader charge of 4.2 electrons. For the Zn-Cr_2O_3 system, one Cr cation is reduced from Cr^{3+} to Cr^{2+} with a computed Bader charge of 4.5 electrons.

As the Ni doped Cr_2O_3 system does not have an oxygen hole, a different behavior is observed. One electron reduces the Ni^{3+} dopant to Ni^{2+} and the other electron partially reduces the two neighboring Cr cations. Computed Bader charges support this: the charge on the Ni atom increases from 14.7 to 15.0 electrons and the two partially reduced Cr cations have computed Bader charges of 4.4 electrons. In examining the reduction of Cr cations in these doped systems, we considered other distorted structures with initial localization of charge on different Cr cations to achieve charge localization on one Cr cation. However all structures relaxed to those described above, thus indicating that these structures are the most favorable for this dopant + oxygen vacancy system.

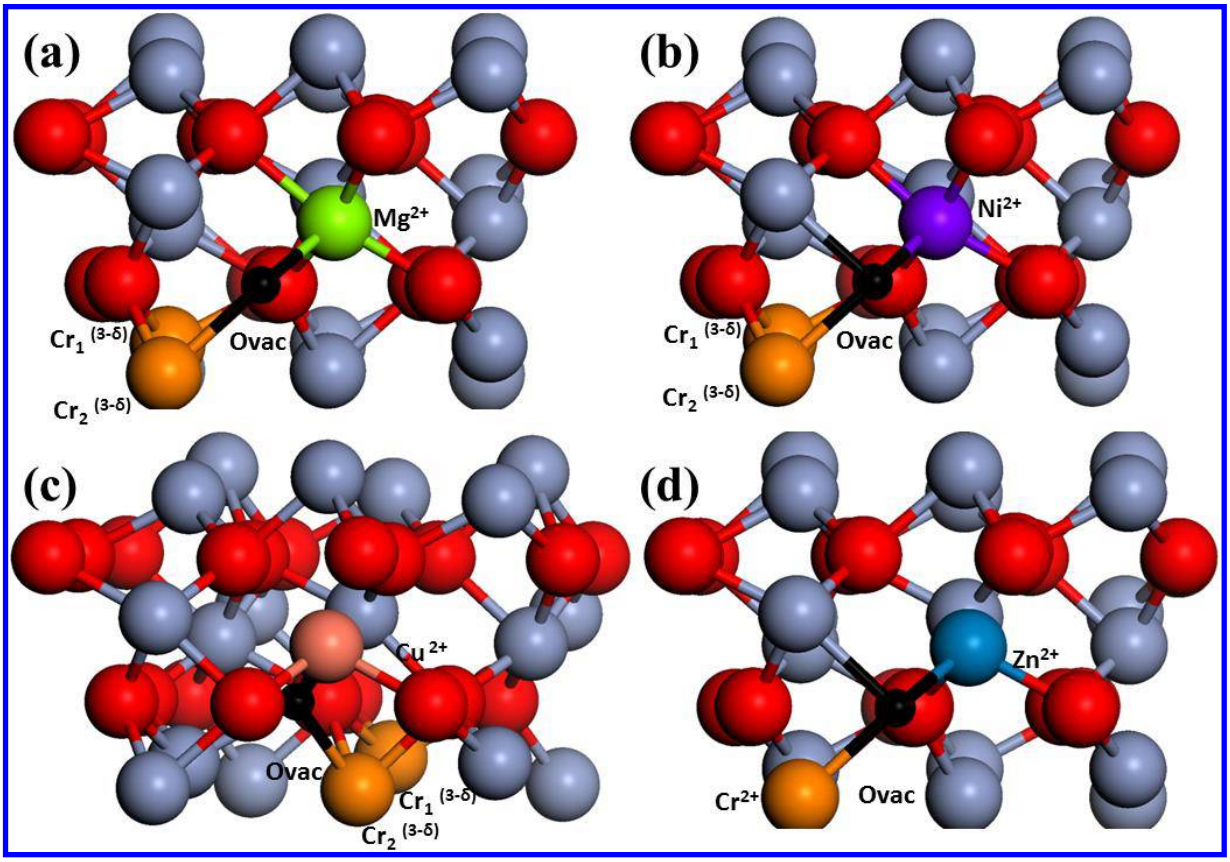

Figure 5: The calculated local geometry after formation of oxygen vacancies in (a) Mg, (b) Ni, (c) Cu and (d) Zn doped Cr2O3. The location of the oxygen vacancy is indicated by the small black sphere, while the partially reduced Cr cations are shown by the orange spheres. The green, purple, brown, and blue spheres show the location of the Mg, Ni, Cu and Zn dopants, respectively, while the lattice positions of the Cr cation and O anions are shown by the grey and red spheres.

The calculated PEDOS plots for each of the doped systems containing an oxygen vacancy are shown in Figure 6. The formation of the oxygen vacancy fills the oxygen hole formed by doping, and there are no O 2p peaks present in the band gap further supporting the description above. The Ni and Cu dopants introduce occupied 3d states into the band gap lying above the top of the VB, where the Ni 3d states raise to 0.4eV above the VB edge and the Cu 3d states remain at the same energy comparing to the doped bulk structure without an Ovac. Comparing the PEDOS for Ni doped Cr_2O_3 with an oxygen

vacancy in Figure 5b, to the PEDOS of Ni doped Cr_2O_3 in Figure 4b, the number of occupied Ni 3d states has increased, which indicates reduction of Ni^{3+} to Ni^{2+} which is also reflected in the Bader charges as they increase from 14.7 to 15 electrons. The bottom panel of Figure 6 shows the PEDOS of the reduced Cr cations that have been identified above and these are labeled Cr_1 and Cr_2. For Mg and Cu doped Cr_2O_3, both partially reduced $Cr^{(3-\delta)+}$ cations introduce occupied β-spin peaks in the band gap around 1eV above the top of the VB, and unoccupied β-spin peaks just below the bottom of the CB around 2eV above the VB edge. The partially reduced $Cr^{(3-\delta)+}$ cations in Ni-Cr_2O_3 have different spin states with Cr_1 being α-spin and Cr_2 β-spin and they introduce defect states into the band gap with occupied and unoccupied peaks below and above the Fermi level. For Zn-Cr_2O_3, the calculated PEDOS for the reduced Cr^{2+} cation shows one occupied β-spin peak around 1eV above the top of the VB and an unoccupied β-spin peak at 2eV above the VB.

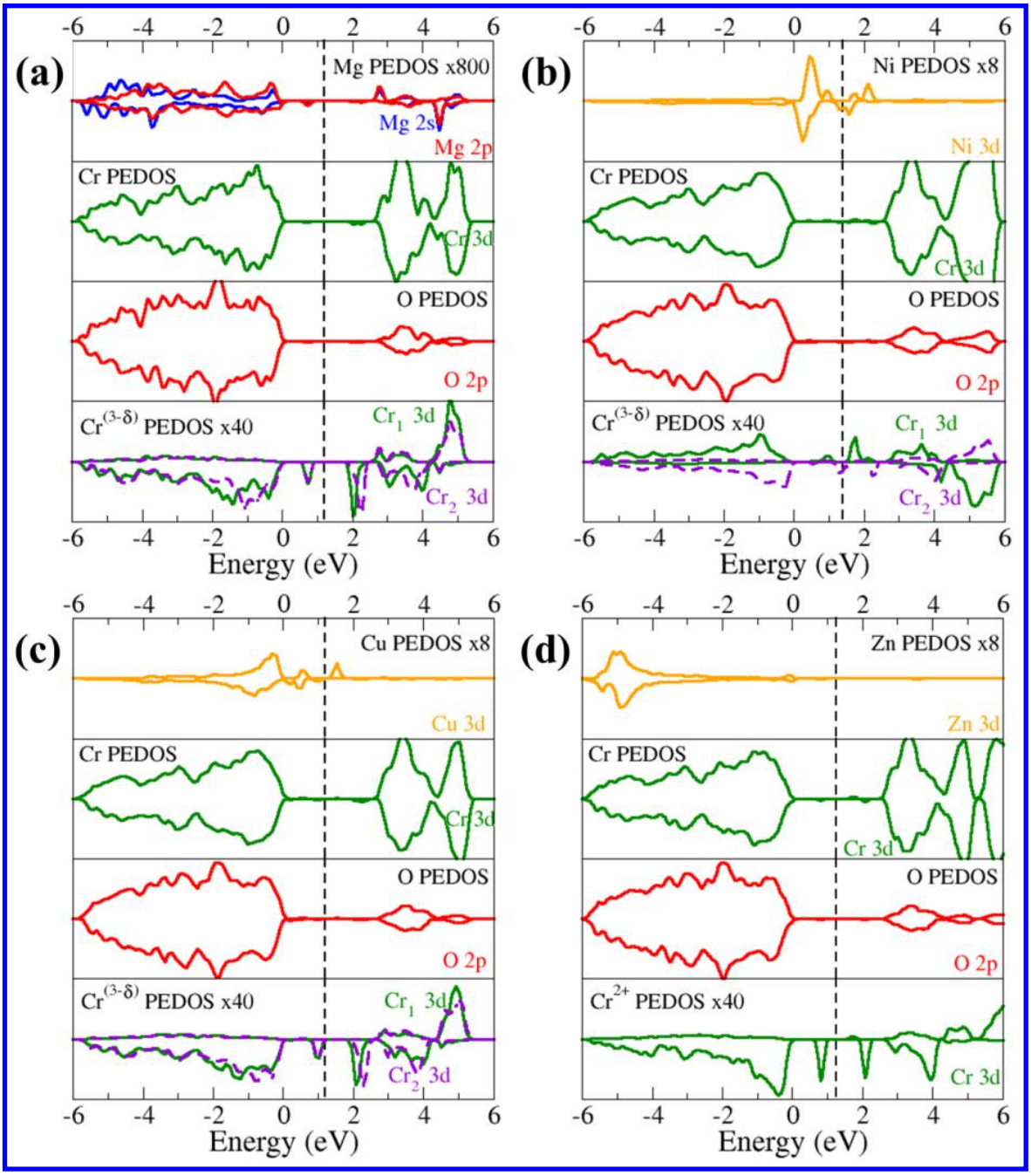

Figure 6: The calculated PEDOS plots for (a) Mg, (b) Ni, (c) Cu and (d) Zn doped Cr_2O_3. The green and red lines show the Cr 3d and O 2p states, while the orange lines show the Ni, Cu and Zn 3d states. The blue and red lines for Mg-Cr_2O_3 show the Mg 2s and 2p states respectively. The bottom panel in each case shows the PEDOS for the reduced Cr cations with the dashed purple lines show the contribution of the different coordinated Cr cation. The top of the VB in each plot is aligned to 0eV and the dashed black line shows the location of the Fermi level.

3.3 Doping the α-Cr_2O_3 bulk lattice with two lower valence dopants: hole formation, charge compensation and active oxygen vacancy formation

We showed in Sec. 3.2 that introducing divalent dopants into the bulk Cr_2O_3 lattice creates holes on neighboring oxygen atoms that are subsequently filled by formation of oxygen vacancies, which form at a lower energy cost than in undoped Cr_2O_3. However the presence of lower valent dopants in bulk Cr_2O_3 can also result in formation of the charge compensating oxygen vacancy, in which two dopants create two holes that are compensated by an oxygen vacancy. In addition, filling the oxygen hole may lead to too low of an Ovac formation energy. We have previously shown that the oxygen vacancy compensated structure is in fact the ground state in lower valent doped CeO_2 and TiO_2[49-52,55,56]. In this section, we therefore study charge compensation in divalent doped bulk Cr_2O_3

The doping of bulk Cr_2O_3 lattice with two divalent dopants is investigated by using the single dopant as a starting structure and substituting different Cr lattice sites with the second dopant to explore the lowest energy configuration for two divalent dopants. The lowest energy structures for two divalent dopants, the charge compensated structured and the active oxygen vacancy, as well as the associated PEDOS plots are shown in Figures 7, 8 , 9 and 10 for Mg, Ni, Cu and Zn and in what follows we describe the dopants individually. Compared to the structures shown in Figures 7 – 10, any other combination of 2 dopants in the Chromia lattice, in particular where dopants are separated, lies *ca.* 3 eV higher in energy.

The second Mg dopant preferentially replaces a Cr cation in the layer above the first dopant, and adopts a similar bonding geometry to the first dopant. The two holes are formed on oxygen sites that lie between the two cationic layers containing Mg. Hole formation is further confirmed by Bader analysis which gives a charge of 7.0 electrons and a spin magnetization of 0.5 on each oxygen species. This is also reflected in the calculated PEDOS as unoccupied O 2p α- and β- spin peaks (overall singlet ground states) are present at 0.5 eV above the VB edge.

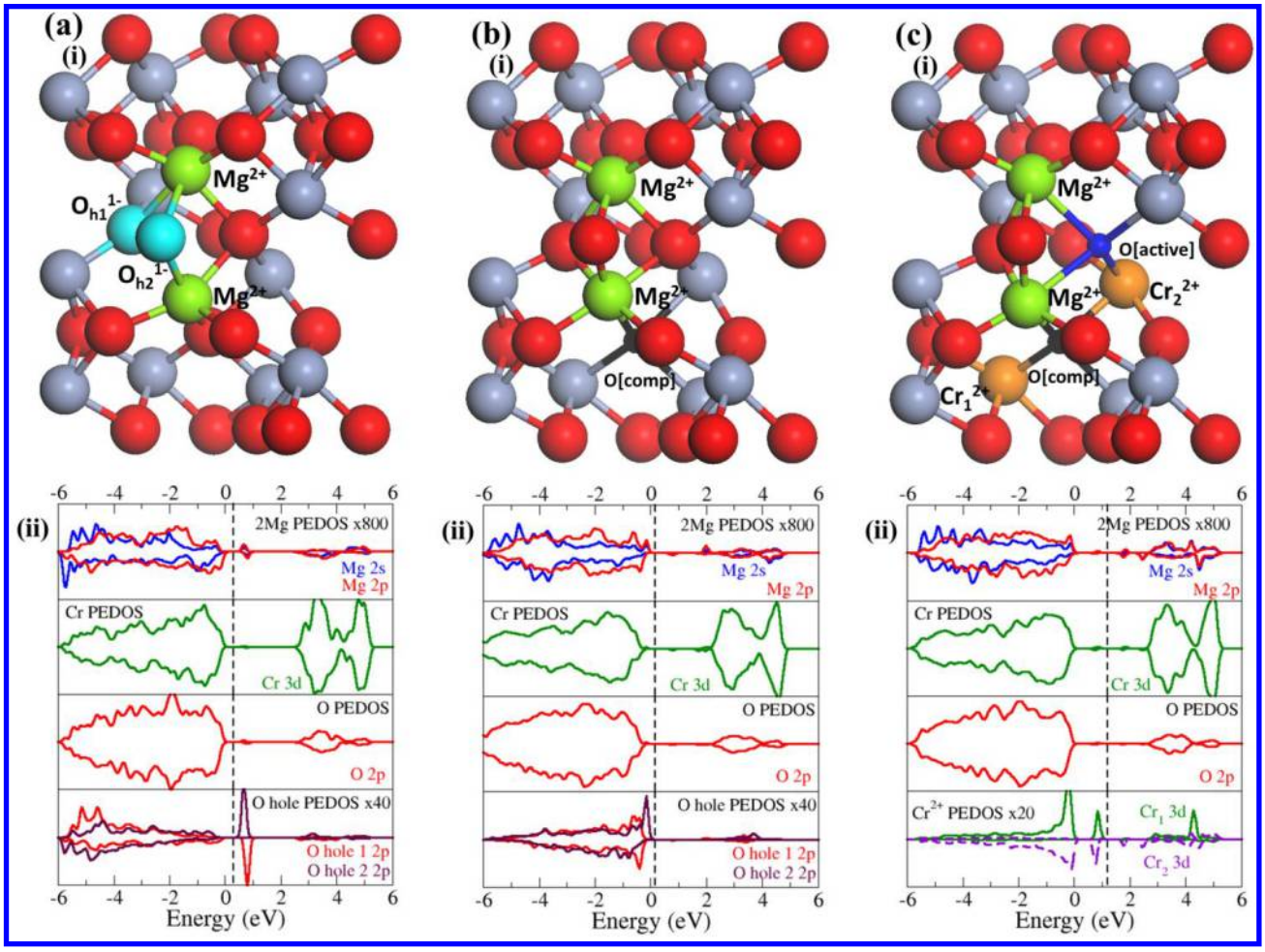

Figure 7: The local atomic structure and calculated PEDOS plots of 2Mg doped Cr_2O_3 for (a) two Mg dopants, (b) charge compensated structure, and (c) active oxygen vacancy. The green, grey, red, light blue and orange spheres show the lattice positions of the Mg dopant, Cr cation, O anion, O atom with hole, and reduced Cr cations respectively. The small black and blue sphere shows the location of the compensated and active oxygen vacancies. For the PEDOS plots, the blue, red and green lines show the s, p and d state contributions to the VB and CB. The top of the VB is aligned to 0eV, and the dashed black line shows the position of the Fermi level.

In determining the charge compensating vacancy we explored different positions for the oxygen vacancy relative to the two Mg dopants and the lowest energy structure for two Mg dopants and a com-

pensated oxygen vacancy is shown in Figure 7(b) with the calculated PEDOS plot shown in Figure 7(b)(ii). The calculated formation energy of the compensating vacancy is +1.43eV for PBE+U, and -2.07eV for HSE. The PBE+U energies would predict that the compensating oxygen vacancy has an energy cost, but the hybrid DFT functional HSE predicts spontaneous oxygen vacancy formation and thus that the charge compensated structure is the stable ground state. This difference between PBE+U has been seen for Mg doped CeO_2 and trivalent doping of TiO_2 where PBE+U does not necessarily predict that the oxygen vacancy is compensating but compensation is stable with the HSE functional [49,51]

The compensating oxygen vacancy prefers to form in the layer below the Mg dopants, and its formation releases two electrons into the system, filling both holes on the neighboring oxygen atoms. The PEDOS shows that the holes are indeed filled as the previously empty O 2p states are now occupied and lie below the Fermi level. This is also supported by the Bader charges, which are 7.3 electrons, consistent with an O^{2-} species. The formation of the compensating oxygen vacancy changes the local geometry of the Mg dopants, with the Mg dopant nearest the vacancy site taking a 5 coordinated square pyramidal geometry.

The removal of second oxygen atom, which will be referred to as the "active" oxygen vacancy and which reduces the system, was explored by removing this oxygen atom from different lattice sites **(**See supplementary information Tables S1 – S4 for the range of computed oxygen vacancy formation energies**)**. The lowest energy configuration for the active oxygen vacancy and the calculated PEDOS are shown in Figure 7(c). The preferred position of the active vacancy is the oxygen site coordinated to the two dopants, forming a dopant-vacancy complex (which is always more favourable than separated dopant and vacancy, Table S5 supplementary information), and it has a calculated formation energy of +2.38eV (PBE+U). The formation of the active oxygen vacancy reduces two neighboring Cr cations from Cr^{3+} to Cr^{2+}; multiple positions of the Cr^{2+} cations were investigated and the lowest energy arrangement is shown in figure 7. Reduction of the two Cr cations was confirmed by Bader analysis for which the calculated charge is 4.5 electrons. The PEDOS plots for the reduced Cr cations in Figure 7(c) shows the Cr 3d peaks in the

VB to CB energy gap, with an α-spin peak associated with the Cr_1 cation and a β-spin peak for the Cr_2 cation.

For Ni doping, the most stable position of the second Ni atom is the next Cr layer above the first Ni dopant, as shown in Figure 8(a) and this Ni takes a three-fold trigonal pyramidal structure; in contrast, the first Ni dopant has a 6 coordinated octahedral bonding environment. Bader charges indicate that the second Ni dopant has an oxidation state of +2, compared to the +3 oxidation state of the first Ni dopant, which is also reflected in the PEDOS plot in Figure 8(a) as we can see two different electronic structures for the dopants. The introduction of a Ni^{2+} dopant on the Cr^{3+} cation lattice sites introduces a hole on a neighboring oxygen atom (indicated by a light blue sphere in Figure 8(a)), which has a computed Bader charge of 7.0 electrons and a spin magnetization of 0.5 electrons. The PEDOS for this oxygen atom in the lower panel of Figure 8(a) shows an unoccupied O 2p peak above the Fermi level. An occupied peak in the PEDOS just below the Fermi level is attributed to the interaction with the Ni 3d states.

The lowest energy structure for the oxygen vacancy compensated system is shown in Figure 8(b) with the position of the compensated vacancy being below and next neighbor to the Ni^{3+} dopant. The calculated formation energy for this oxygen vacancy is +2.93eV (PBE+U) and –1.08 (HSE) with the negative formation energy for HSE predicting that charge compensation takes place. The two electrons released fill the oxygen hole and reduced the previous Ni^{3+} dopant to Ni^{2+} (shown as a light purple sphere in Figure 8), so that both dopants now take their preferred +2 oxidation state. The second Ni dopant remains in a trigonal pyramidal geometry and the first Ni dopant now takes a square pyramidal geometry due to loss of the compensating oxygen. The PEDOS in Figure 8(b) confirms that the oxygen hole is filled and the reduction of Ni^{3+} to Ni^{2+} is reflected in the upper panel of the PEDOS as the previously empty Ni states now become filled and fall below the Fermi level; the PEDOS for both Ni dopants have similar characteristics suggesting they exist in the same oxidation state. The filling of the hole on the oxygen atom and the reduction of the Ni dopant is supported by Bader analysis and spin magnetiza-

tion: the Bader charge for the O atom increase to 7.3 electrons, with zero spin magnetization, and the original Ni^{3+} dopant shows a Bader charge of 14.9 electrons (from 14.6 electrons), which is similar to the Bader charge for the other Ni^{3+} 14.8 electrons.

The most stable position for the active oxygen vacancy for Ni-doped Cr_2O_3 is shown in Figure 8(c), in which the vacancy site lies above and next neighbor to the second Ni dopant (indicated by the blue sphere in Figure 8(c). The calculated formation energy of the active vacancy is +2.53 eV (PBE+U), which is lower than undoped Cr_2O_3, suggesting that Ni doping can enhance oxygen vacancy formation in bulk Cr_2O_3. The removal of the second oxygen atom changes the coordination of the nearest Ni^{2+} dopant from a trigonal pyramidal geometry to a four coordinated square planar geometry that is stable for Ni as a dopant.[51] The other Ni^{2+} dopant maintains its coordination environment. The formation of the active oxygen vacancy reduces two neighboring Cr cations from Cr^{3+} to Cr^{2+} and the location of the Cr^{2+} is indicated by the orange spheres in Figure 8(c). The PEDOS for these cations is shown in the lower panel of Figure 8(c), with the appearance of Cr 3d β-spin peaks in the VB to CB energy gap for both cations. The reduction of Cr from Cr^{3+} to Cr^{2+} is further supported by computed Bader charges, which are 4.5 electrons, and different PEDOS plots are shown for the different coordination environments of the reduced Cr cations.

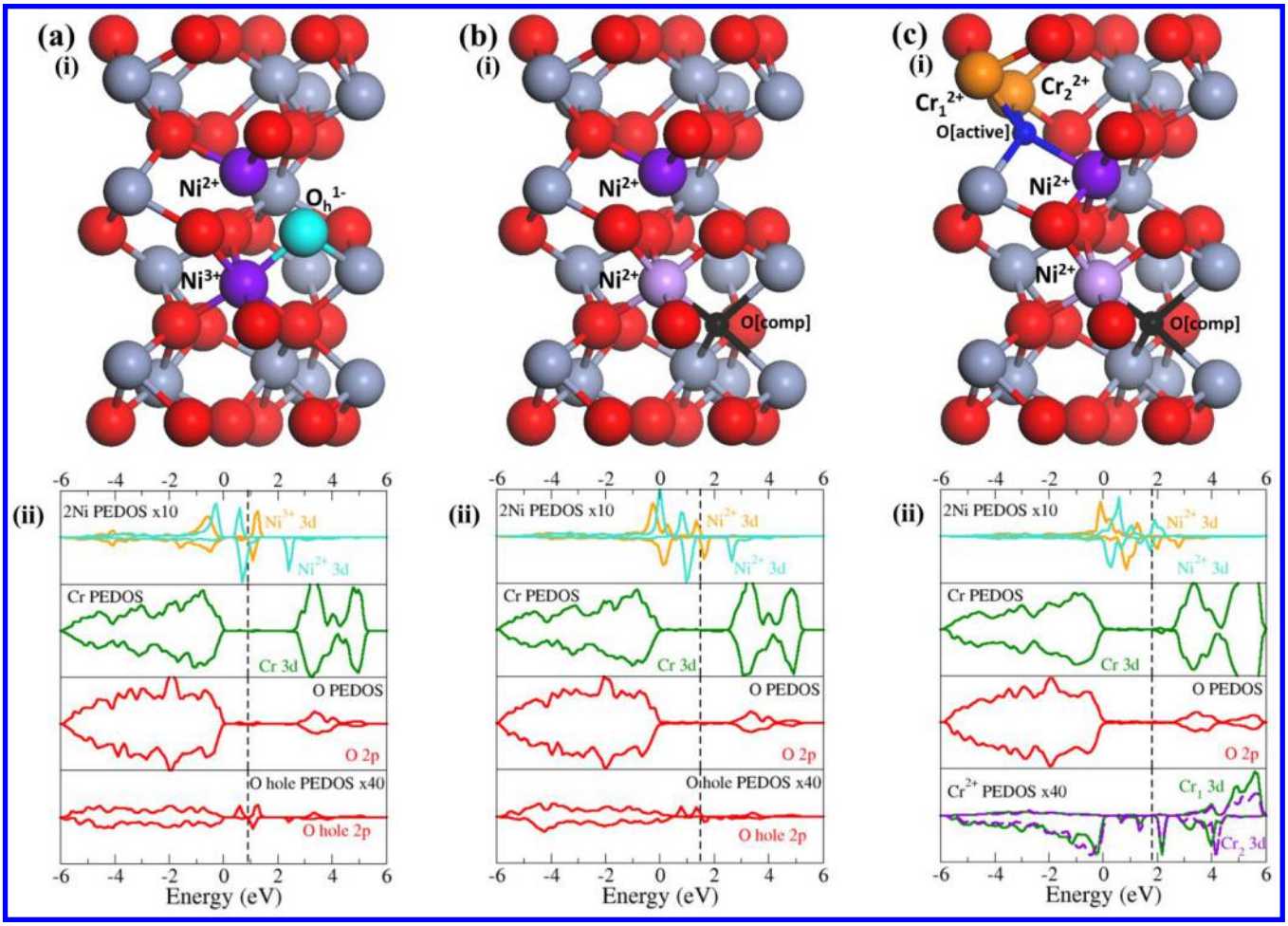

Figure 8: The local atomic structure and calculated PEDOS for 2Ni doped Cr_2O_3 for (a) two Ni dopants, (b) charge compensated structure, and (c) active oxygen vacancy. The purple, grey, red, light blue and orange spheres show the lattice positions of the Ni dopant, Cr cation, O anion, O atom with hole, and reduced Cr cations respectively. The small black and blue sphere shows the location of the compensated and active oxygen vacancies. For the PEDOS plots, green and red lines show the Cr 3d and O 2p state contributions to the VB and CB, while the light blue, orange lines show the contributions of the different Ni 3d states. The top of the VB is aligned to 0eV, and the dashed black line shows the position of the Fermi level.

The lowest energy structures for two Cu dopants, the oxygen vacancy compensated and active oxygen vacancy structures are shown in Figure 9(a),(b),(c). For two Cu dopants, the most stable site for the second Cu dopant is in the next Cr layer above the first dopant. The Cu dopants have similar coordination environments - both are three-fold coordinated. The introduction of the second Cu dopant results in formation of a hole on a neighboring oxygen and the sites of the oxygen holes are shown by the light blue spheres in Figure 9(a). The holes lie in different oxygen layers, but each hole neighbors a Cu site.

The PEDOS plot for Cr_2O_3 with two Cu dopants is shown in the top panel of Figure 9(a). The PEDOS features for the two Cu dopants are similar as they are in similar bonding environments. The formation of the holes on the neighboring oxygen atoms is seen in the lower panel of the PEDOS plots, with the appearance of unoccupied O 2p peaks above the Fermi level. Bader charges and spin magnetizations further support hole formation with a computed charge of 7.0 electrons on each oxygen atoms and a computed spin magnetization of 0.5 electrons.

The preferential site for the compensating oxygen vacancy is in the oxygen layer between the two Cu dopants as shown in Figure 9(b). The calculated formation energy for the oxygen vacancy is +0.84 eV (PBE+U) and -2.31 eV (HSE) with the negative energy from HSE indicating spontaneous oxygen vacancy formation and charge compensation. The removal of this oxygen atom fills the two holes formed by Cu doping, and changes the local coordination geometry of both Cu dopants. Both Cu dopants change from 3 fold trigonal pyramidal environment to a 4 fold coordinated environment. The lower panel of the PEDOS plot in Figure 9(b) shows that the previous oxygen hole peak on these are now occupied, lying below the Fermi level. In addition, the Cu dopants maintain their +2 oxidation states. The filling of the holes is further confirmed by Bader charges, which are computed to be 7.3 electrons on each oxygen species and the computed spin magnetization is 0.0 electrons.

The active oxygen vacancy is preferentially found on the next neighbor position to the Cu dopant in the lower cationic layer as shown by the blue sphere in Figure 9(c),. The calculated formation energy is +2.86eV (PBE+U). The removal of the second oxygen atom reduces a neighboring Cr^{3+} to

Cr^{2+} as indicated by the orange sphere in Figure 9(c), and the second electron reduces the neighbouring Cu^{2+} species to Cu^{1+} as indicated by the green sphere. The Cu 3d PEDOS for this atom in the top panel of the PEDOS plot in Figure 9(c) shows that these states fall below the Fermi level when compared to the same Cu 3d states for the charge compensated structure in Figure 9(b), indicative of Cu^{2+} reduction to Cu^{+}. This is supported by Bader charge analysis with a change in the Cu charge from 15.9 electrons to 16.3 electrons. The bottom panel of the PEDOS for the active vacancy shows the appearance of a Cr 3d peak in the VB to CB energy gap around 1 eV above the VB edge, which is consistent with reduction to Cr^{2+}. The Bader charge for the reduced Cr atom is 4.5 electrons, consistent with a Cr^{2+} species.

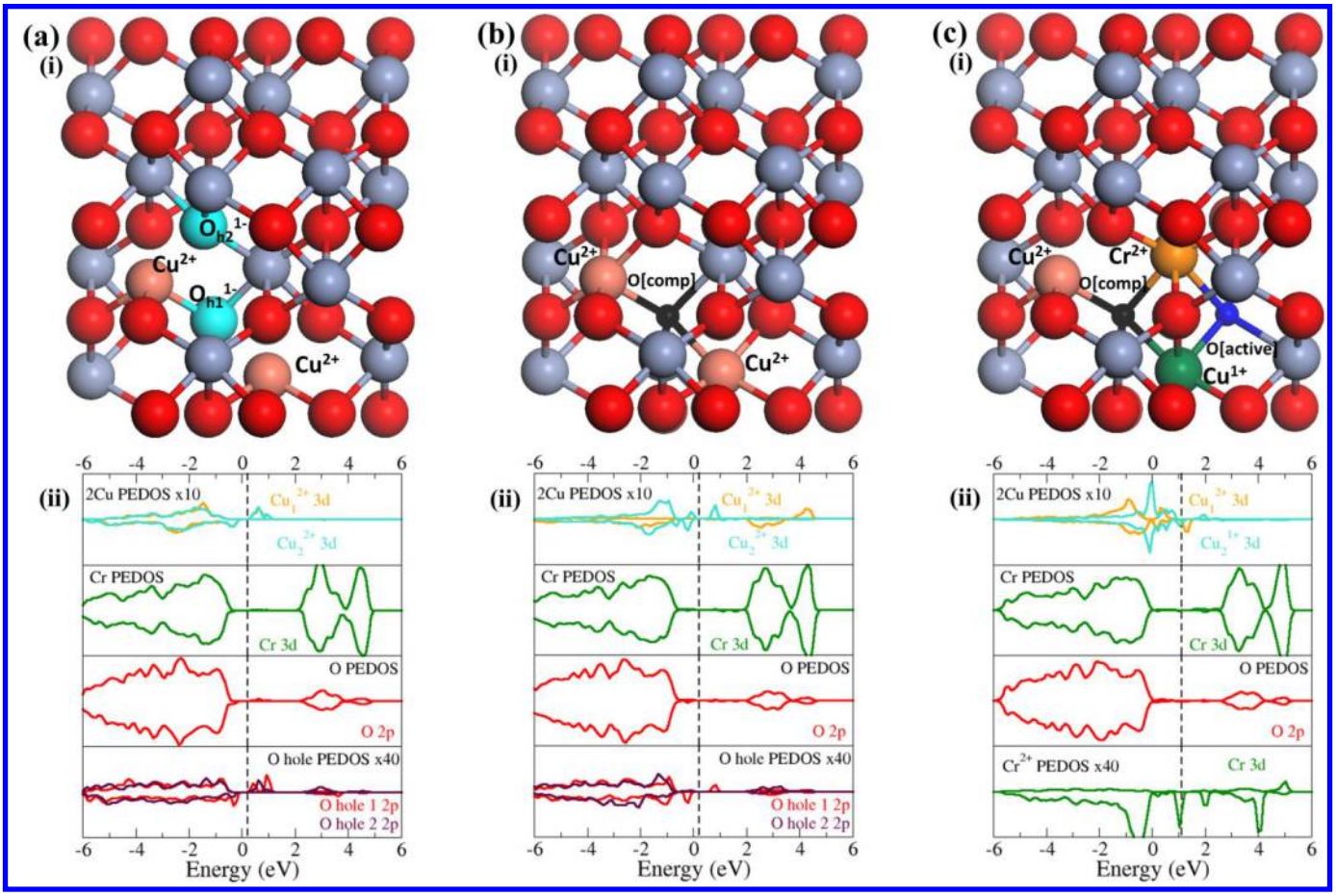

Figure 9: The local atomic structure and calculated PEDOS for 2Cu doped Cr_2O_3 for (a) two Cu dopants, (b) charge compensated structure, and (c) active oxygen vacancy. The brown, grey, red, light blue and orange spheres show the lattice positions of the Cu dopant, Cr cation, O anion, O atom with hole, and reduced Cr cations respectively. The small black and blue sphere shows the location of the compensated and active oxygen vacancies. For the PEDOS plots, green and red lines show the Cr 3d and O 2p state contributions to the VB and CB, while the light blue, orange lines show the contributions of the different Cu 3d states. The top of the VB is aligned to 0eV, and the dashed black line shows the position of the Fermi level.

Figure 10(a) shows the atomic structure for two Zn dopants in Cr_2O_3. The second Zn dopant prefers to locate in the cationic layer below the first Zn dopant and adopts a 5 coordinated trigonal bipyramidal geometry; the first Zn dopant maintains its 3 fold trigonal pyramidal geometry. The Zn divalent dopants produce two holes on next neighbor oxygen atoms, indicated by the light blue spheres in Figure 10(a). The calculated PEDOS is shown in Figure 10(a). The unoccupied O 2p peaks typical of the oxygen hole appear above the Fermi level and hole formation is further supported by Bader charges of 7.0 electrons on each oxygen and a computed spin magnetization of 0.5 electrons.

The lowest energy structure for the charge compensated structure is shown in Figure 10(b). The preferred location of the vacancy is a site that bridges the two Zn dopants, indicated by the black sphere in Figure 10 (b). The removal of this oxygen modifies the coordination of both Zn dopants - the Zn dopant in the upper Cr layer maintains the 3 coordinated trigonal pyramidal geometry but bonds to different O atoms, while the Zn dopant in the lower Cr layer changes to have a 3 fold trigonal pyramidal bonding geometry. The calculated formation energy for this vacancy is +0.15eV (PBE+U) and -3.62eV (HSE), which indicates that it forms to compensate the dopants. The compensating vacancy fills the two holes on the neighboring oxygen atoms, which is reflected in the PEDOS plot in Figure 10(b); the lower panel shows that the previously unoccupied O 2p states are now occupied and lie below the Fermi level. The Bader charges of 7.3 electrons on each oxygen further support the filling of the holes and the computed spin magnetizations are 0.0 electrons.

The structure of the most stable active oxygen vacancy is shown in Figure 10(c). The vacancy prefers to be located above the upper Zn dopant, as indicated by the blue sphere. The removal of this oxygen atom changes the coordination environment of the upper Zn dopant to a 3 fold trigonal planar geometry, while the lower Zn dopant is unchanged. The calculated energy for the formation of the active vacancy is +3.21eV and two Cr cations are reduced from Cr^{3+} to Cr^{2+}. One Cr is nearest neighbor to the active vacancy and the reduced Cr^{2+} is in a next nearest neighbor site. The PEDOS plot in Figure 10(c) shows two occupied Cr 3d peaks in the VB to CB energy gap, at around 0.7 eV and 0.9 eV, and unoccu-

pied Cr 3d peaks between 1.9 and 2.1 eV above the top of the VB. The higher energy PEDOS occupied peak is associated with the Cr^{2+} cation that is nearest neighbor to the active vacancy. The two reduced Cr^{2+} cations have Bader charges of 4.5 electrons, and computed spin magnetizations of 3.5 electrons.

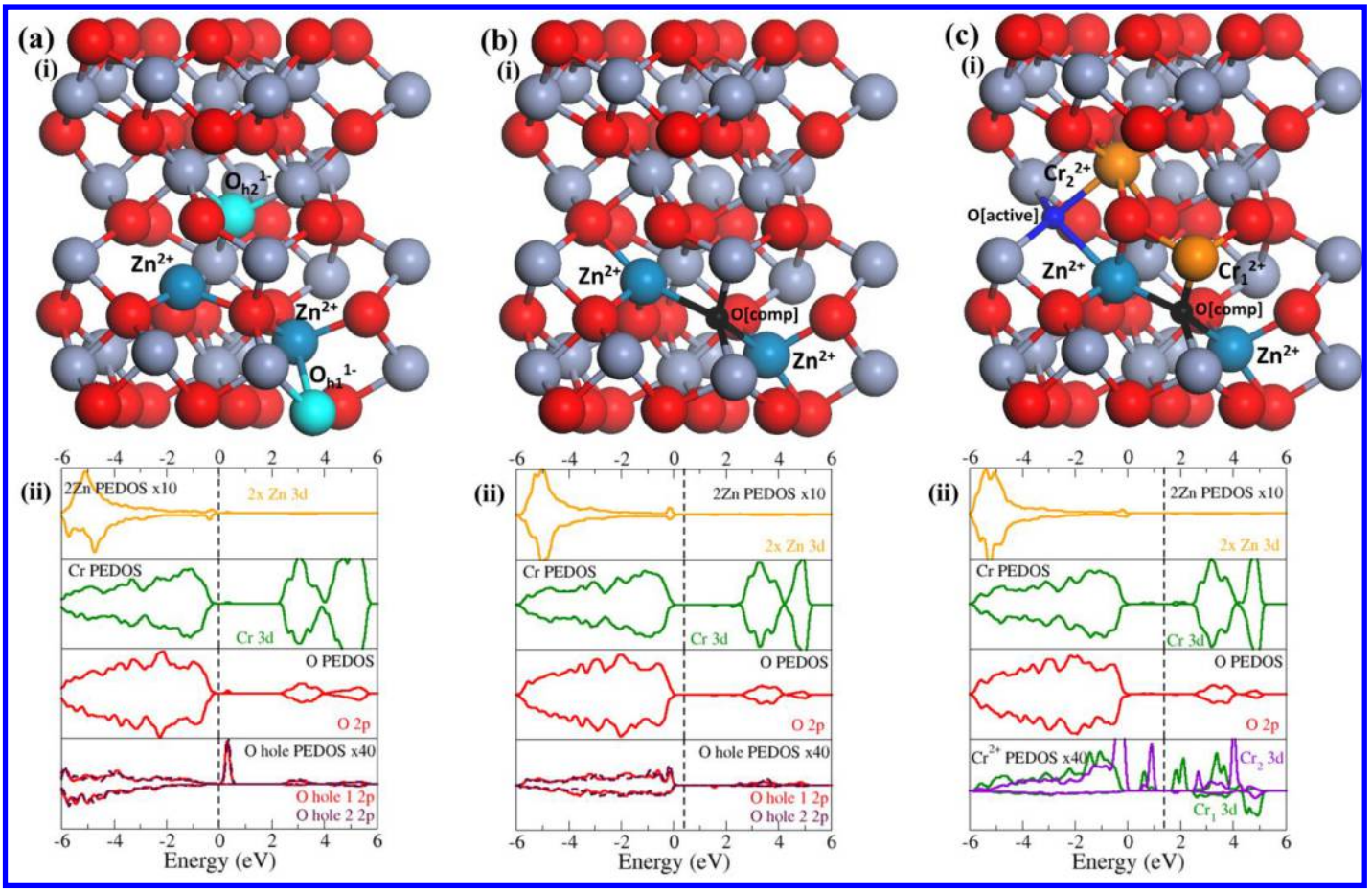

Figure 10: The local atomic structure and calculated PEDOS for 2Zn doped Cr_2O_3 for (a) two Zn dopants, (b) charge compensated structure, and (c) active oxygen vacancy. The dark blue, grey, red, light blue and orange spheres show the lattice positions of the Zn dopant, Cr cation, O anion, O atom with hole, and reduced Cr cations respectively. The small black and blue sphere shows the location of the compensated and active oxygen vacancies. For the PEDOS plots, orange, green and red lines show the Zn 3d, Cr 3d and O 2p state contributions to the VB and CB, while the green and purple lines show the contributions of the different Cr^{2+} 3d states. The top of the VB is aligned to 0eV, and the dashed black line shows the position of the Fermi level.

4. Discussion:

Doping of bulk α-Cr_2O_3 with LV dopants and the effect on formation of potentially active oxygen vacancies was investigated using DFT, within the PBE+U formalism. We have explored two approaches to this question: the widely used approach of doping with one metal cation on the Cr site and computing the formation energy of an oxygen vacancy, and substitutional doping of Cr_2O_3 with a charge compensated structure in which two metal dopants are compensated with an oxygen vacancy, from which the second oxygen removed forms the active oxygen vacancy.

In doping the Cr_2O_3 lattice with a single divalent dopant, an oxygen hole is formed on a neighboring oxygen atom due to the dopant having an oxidation state of one less than Cr^{3+}, the exception being Ni which forms Ni^{3+}. Upon formation of an oxygen vacancy the hole state on this oxygen atom was filled and two nearest neighbor Cr^{3+} cations were partially reduced to $Cr^{(3-\delta)+}$. The calculated energies for oxygen vacancy formation showed that doping in this scheme greatly enhances vacancy formation compared to undoped Cr_2O_3, with Cu doping giving the lowest vacancy formation energy, as shown in Table 3; the cost of forming an oxygen vacancy is lowered by over 2 eV.

In studying the charge compensated system, we introduce two divalent dopants onto two Cr sites in Cr_2O_3 to create two holes on two oxygen atoms, and the formation of an oxygen vacancy releases electrons to fill these holes; this is shown to be spontaneous from a HSE level calculation of the formation energy, so that this is the ground state of divalent doped Cr_2O_3. The lattice is now charge neutral and the removal of a second oxygen atom is a model for the catalytically active oxygen vacancy. This process reduces two Cr^{3+} cations to Cr^{2+} cations, with the exception of Cu doping, and the computed formation energies for each dopant in this scheme are compared to the other scheme in Table 3. Doping of bulk Cr_2O_3 with these divalent dopants enhances oxygen vacancy formation compared to undoped Cr_2O_3, with Mg-doped Cr_2O_3 having the lowest formation energy.

Table 3: A comparison for the different approaches to investigate LV doping of bulk Cr_2O_3 to promote oxygen vacancy formation. The column indicated E[Ovac] is without charge compensation and the column indicated E[active] is with charge compensation.

	M-Cr_2O_3 E[Ovac] (eV)	2M-Cr_2O_3 E[active] (eV)
Undoped Cr_2O_3	4.11	4.11
Mg doped	2.53	2.38
Ni doped	2.45	2.53
Cu doped	1.87	2.86
Zn doped	2.88	3.21

Comparing the two approaches to determining the oxygen vacancy formation energy of divalent doping of Cr_2O_3, using a single metal dopant generally results in a lower formation energy than using the charge compensated structure, while for Ni doping this is nearly the same (0.08eV difference). From work on other doped oxides, this can be attributed to the fact that the vacancy in the first case will compensate the hole which is a favorable process. This can lead to spurious results in terms of measuring reactivity by oxygen vacancy formation and also PBE+U can give different results to HSE06. The formation of the oxygen vacancy also partially reduces two Cr cations (with one electron), which is not observed when the active vacancy is formed in the compensated structure, where two fully reduced Cr cations are produced. Single metal doping of the bulk lattice with LV cations predicts that Cu has the lowest oxygen vacancy formation energy, while the formation of the active vacancy from the compensated structure indicates that Mg gives the lowest energy for vacancy formation.

Ni doping is the exception to this mechanism as it can take a Ni^{3+} oxidation state in the singly doped structure and Ni^{2+} in the compensated structure. The presence of Ni^{3+} suggests that it may not require charge compensation; however it can be argued that the more predominant oxidation state for Ni is +2

which is found in the charge compensated structure. The oxygen vacancy formation energies for either Ni-doped Cr_2O_3 structure are practically the same, which indicate both approaches are consistent for Ni doping of Cr_2O_3. This can also imply that at higher concentrations of Ni doping in Cr_2O_3, Ni^{2+} dopants will be present, while at lower concentrations Ni^{3+} is present. The formation or otherwise of these oxidation states can be identified using X-ray spectroscopies to discriminate between the two possible Ni oxidation states.

Differences between dopants with possible variable oxidation states (Ni, Cu) and non-reducible dopants (Mg, Zn) are also apparent. As the compensated structure is the correct electronic ground state for the divalent doped Cr_2O_3, the formation of the active vacancy shows that the non-reducible dopants allow reduction of two surrounding Cr cations creating electron donor Cr 3d peaks in the band gap, while the Ni and Cu dopants themselves become reduced along with a Cr cation. This leads to a mixture of metal and Cr 3d states contributing to the donor levels in the band gap. This can only be properly described from the compensated structure. Investigating oxygen vacancy formation in Cr_2O_3 from LV doping of the bulk lattice by doping with a single divalent dopant and removing an oxygen atom is insufficient in describing the correct ground state electronic structure, and two divalent dopants with a compensating vacancy (charge neutral system) must be used as the basis for investigating the correct ground state electronic structure for oxygen vacancy formation.

5. Conclusion:

Density functional theory calculations using the Perdew-Burke-Ernzerhof functional and a Hubbard +U correction applied to the Cr 3d and O 2p states (PBE+U) have been used to investigate doping of the bulk α-Cr_2O_3 lattice with lower valence dopants, namely divalent Mg, Ni, Cu and Zn to examine any effect on promoting oxygen vacancy formation. We showed that doping the bulk lattice with a single divalent dopant creates a hole state on the neighboring oxygen atom; however, this provides the incor-

rect description of the ground state electronic structure for studies of oxygen vacancy formation because the stable ground state is in fact one in which the two oxygen holes formed by incorporating two dopants are compensated by forming an oxygen vacancy. This gives a charge neutral system, which is then used to study formation of active oxygen vacancies. In addition, we find that dopants prefer to be found on neighboring Cr lattice sites, with any other distribution being significantly less favorable.

The removal of a second oxygen atom, that is, the active vacancy, reduces two Cr^{3+} cations to Cr^{2+}, with the exception of Cu, and is therefore the correct description of the ground state electronic structure for an oxygen vacancy for each of the doped lattices. All dopants are shown to promote oxygen vacancy formation over undoped bulk Cr_2O_3, with Mg doping giving the lowest formation energy.

The reducibility of the dopant is also seen to have an impact on the doping mechanism and active vacancy formation in the bulk lattice, as the non-reducible Mg and Zn metals allow reduction of surrounding Cr cations, while both Cu and Ni become reduced along with one Cr cation. This may have implications in the use of doped Cr_2O_3 as a potential candidate in the areas of photochemistry and reaction catalysis by promoting formation of multiple reduced cation species in the same material.

Supporting Information

SI contains the calculated energies for each of the tested oxygen vacancy sites, along with the most stable site shown in the main article, and the calculated energies for the metal doped Chromia complex $[M_x: Cr_{(2-x)}O_{(3-y)}]$ relative to a separated dopant metal and $[V_O^{**} + 2e`]$ pair.

AUTHOR INFORMATION

Corresponding Author

*email: john.carey@tyndall.ie, Michael.nolan@tyndall.ie

Tel: +353 (0)21 234 6984

Author Contributions

All authors have given approval to the final version of the manuscript.

ACKNOWLEDGMENT

John Carey and Michael Nolan acknowledge funding from the European FP7 NMP 2013 project BIOGO (grant no: 604296) (Catalytic partial oxidation of biogas and reforming of pyrolysis oil for synthetic gas production and conversion into fuels, www.biogo.eu). Computational resources are provided by the Science Foundation Ireland (SFI) funded Irish Centre for High-end Computing (ICHEC) and by SFI funded resources at Tyndall. We also acknowledge support from COST ACTION CM1104 "Reducible oxides: structure and function".

Funding Sources

This work is funded by the European Framework 7 BIOGO project (grant no: 604296) *(Catalytic partial oxidation of biogas and reforming of pyrolysis oil for synthetic gas production and conversion into fuels* www.biogo.eu),

REFERENCES

(1) Popovici, N.; Paramês, M. L.; Da Silva, R. C.; Monnereau, O.; Sousa, P. M.; Silvestre, A. J.; Conde, O., KrF Pulsed Laser Deposition of Chromium Oxide Thin Films from Cr_8O_{21} Targets, *Appl. Phys. A-Mater.,* **2004**, *79*, 1409-1411.

(2) Corliss, L. M.; Hastings, J. M.; Nathans, R.; Shirane, G., Magnetic Structure of Cr_2O_3, *J. Appl. Phys.,* **1965**, *36*, 1099-1100.

(3) Brown, P. J.; Forsyth, J. B.; Lelièvre-Berna, E.; Tasset, F., Determination of the Magnetization Distribution in Cr_2O_3 using Spherical Neutron Polarimetry, *J. Phys.: Condens. Matter,* **2002**, *14*, 1957.

(4) Lebreau, F.; Islam, M. M.; Diawara, B.; Marcus, P., Structural, Magnetic, Electronic, Defect, and Diffusion Properties of Cr_2O_3: A DFT+U Study, *J. Phys. Chem. C,* **2014**, *118*, 18133-18145.

(5) Maldonado, F.; Rivera, R.; Stashans, A., Structure, Electronic and Magnetic Properties of Ca-doped Chromium Oxide Studied by the DFT Method, *Physica B,* **2012**, *407*, 1262-1267.

(6) Rohrbach, A.; Hafner, J.; Kresse, G., *Ab initio* Study of the (0001) Surfaces of Hematite and Chromia: Influence of Strong Electronic Correlations, *Phys. Rev. B,* **2004**, *70*, 125426.

(7) Yuzheng, G.; Stewart, J. C.; John, R., Electronic and Magnetic Properties of Ti_2O_3 , Cr_2O_3 , and Fe_2O_3 Calculated by the Screened Exchange Hybrid Density Functional, *J. Phys.: Condens. Matter,* **2012**, *24*, 325504.

(8) Maldonado, F.; Novillo, C.; Stashans, A., Ab Initio Calculation of Chromium Oxide Containing Ti Dopant, *Chem. Phys.,* **2012**, *393*, 148-152.
(9) Zimmermann, R.; Steiner, P.; Hüfner, S. In *Proc. 11th Intern. Conf. Vac. UV Rad. Phys.* ; Miyahara, T., Azuma, Y., Watanabe, M., Ishii, T., Eds.; Elsevier: Amsterdam, 1996, p 49-52.
(10) Uozumi, T.; Okada, K.; Kotani, A.; Zimmermann, R.; Steiner, P.; Hüfner, S.; Tezuka, Y.; Shin, S., Theoretical and Experimental Studies on the Electronic Structure of M_2O_3 (M = Ti, V, Cr, Mn, Fe) Compounds by Systematic Analysis of High-Energy Spectroscopy, *J. Electron. Spectrosc. Relat. Phenom.,* **1997**, *83*, 9-20.
(11) Nakayama, O.; Ikenaga, N.; Miyake, T.; Yagasaki, E.; Suzuki, T., Production of Synthesis Gas from Methane Using Lattice Oxygen of NiO−Cr_2O_3−MgO Complex Oxide, *Ind. Eng. Chem. Res.,* **2010**, *49*, 526-534.
(12) El-Molla, S. A., Surface and Catalytic Properties of Cr_2O_3/MgO System Doped with Manganese and Cobalt Oxides, *Appl. Catal. A,* **2005**, *280*, 189-197.
(13) Calverley, E. M.; Smith, K. J., Kinetic Model for Alcohol Synthesis over a Promoted Copper/Zinc Oxide/Chromium Oxide (Cr_2O_3) Catalyst, *Ind. Eng. Chem. Res.,* **1992**, *31*, 792-803.
(14) Cline, J. A.; Rigos, A. A.; Arias, T. A., Ab Initio Study of Magnetic Structure and Chemical Reactivity of Cr_2O_3 and Its (0001) Surface, *J. Phys. Chem. B,* **2000**, *104*, 6195-6201.
(15) Brady, M. P.; Pint, B. A.; Lu, Z. G.; Zhu, J. H.; Milliken, C. E.; Kreidler, E. D.; Miller, L.; Armstrong, T. R.; Walker, L. R., Comparison of Oxidation Behavior and Electrical Properties of Doped NiO- and Cr_2O_3 -Forming Alloys for Solid-Oxide, Fuel-Cell Metallic Interconnects, *Oxid Met,* **2006**, *65*, 237-261.
(16) Hu, J.; Li, H.; Huang, X.; Chen, L., Improve the Electrochemical Performances of Cr_2O_3 Anode for Lithium Ion Batteries, *Solid State Ionics,* **2006**, *177*, 2791-2799.
(17) Kohli, N.; Singh, O.; Singh, R., Sensing Behaviour of Tin Doped Chromium Oxide Gas Sensor Toward Ethanol, *Appl. Phys. A,* **2012**, *109*, 585-590.
(18) Chen, X.; Hou, P. Y.; Jacobson, C. P.; Visco, S. J.; De Jonghe, L. C., Protective Coating on Stainless Steel Interconnect for SOFCs: Oxidation Kinetics and Electrical Properties, *Solid State Ionics,* **2005**, *176*, 425-433.
(19) Liu, Y.; Chen, D., Protective Coatings for Cr_2O_3 -Forming Interconnects of Solid Oxide Fuel Cells, *Int. J. Hydrogen Energy,* **2009**, *34*, 9220-9226.
(20) Xiao, M.; Zhao, M.; Lang, X.; Zhu, Y.; Jiang, Q., Improvement of Electromigration Reliability and Diffusion of Cu Films using Coherent Cu (111)/Cr_2O_3 (0001) Interfaces, *Chem. Phys. Lett.,* **2012**, *542*, 85-88.
(21) Batzill, M.; Morales, E. H.; Diebold, U., Influence of Nitrogen Doping on the Defect Formation and Surface Properties of TiO_2 Rutile and Anatase, *Phys. Rev. Lett.,* **2006**, *96*, 026103.
(22) Gordon, T. R.; Cargnello, M.; Paik, T.; Mangolini, F.; Weber, R. T.; Fornasiero, P.; Murray, C. B., Nonaqueous Synthesis of TiO_2 Nanocrystals using TiF_4 to Engineer Morphology, Oxygen Vacancy Concentration, and Photocatalytic Activity, *J. Am. Chem. Soc.,* **2012**, *134*, 6751-6761.
(23) Nakamura, I.; Negishi, N.; Kutsuna, S.; Ihara, T.; Sugihara, S.; Takeuchi, K., Role of Oxygen Vacancy in the Plasma-treated TiO_2 Photocatalyst with Visible Light Activity for NO Removal, *J. Mol. Catal. A: Chem.,* **2000**, *161*, 205-212.
(24) Schaub, R.; Wahlström, E.; Rønnau, A.; Lægsgaard, E.; Stensgaard, I.; Besenbacher, F., Oxygen-mediated Diffusion of Oxygen Vacancies on the TiO_2 (110) Surface, *Science,* **2003**, *299*, 377-379.
(25) Skorodumova, N.; Simak, S.; Lundqvist, B. I.; Abrikosov, I.; Johansson, B., Quantum Origin of the Oxygen Storage Capability of Ceria, *Phys. Rev. Lett.,* **2002**, *89*, 166601.
(26) Fornasiero, P.; Dimonte, R.; Rao, G. R.; Kaspar, J.; Meriani, S.; Trovarelli, A.-; Graziani, M., Rh-loaded CeO_2 -ZrO_2 Solid-solutions as Highly Efficient Oxygen Exchangers: Dependence of the Reduction Behavior and the Oxygen Storage Capacity on the Structural-properties, *J. Catal.,* **1995**, *151*, 168-177.

(27) Nolan, M.; Fearon, J. E.; Watson, G. W., Oxygen Vacancy Formation and Migration in Ceria, *Solid State Ionics,* **2006**, *177*, 3069-3074.
(28) Nolan, M.; Parker, S. C.; Watson, G. W., The Electronic Structure of Oxygen Vacancy Defects at the Low Index Surfaces of Ceria, *Surf. Sci.,* **2005**, *595*, 223-232.
(29) Catlow, C. R. A.; Corish, J.; Hennessy, J.; Mackrodt, W. C., Atomistic Simulation of Defect Structures and Ion Transport in α-Fe_2O_3 and α-Cr_2O_3, *J. Am. Ceram. Soc.,* **1988**, *71*, 42-49.
(30) Qin, P.; Fang, G.; He, Q.; Sun, N.; Fan, X.; Zheng, Q.; Chen, F.; Wan, J.; Zhao, X., Nitrogen Doped Amorphous Chromium Oxide: Stability Improvement and Application for the Hole-transporting Layer of Organic Solar Cells, *Sol. Energy Mater. Sol. Cells,* **2011**, *95*, 1005-1010.
(31) Qin, P.; Fang, G.; Sun, N.; Fan, X.; Zheng, Q.; Chen, F.; Wan, J.; Zhao, X., Organic Solar Cells with P-type Amorphous Chromium Oxide Thin Film as Hole-transporting Layer, *Thin Solid Films,* **2011**, *519*, 4334-4341.
(32) Cao, H.; Qiu, X.; Liang, Y.; Zhao, M.; Zhu, Q., Sol-gel Synthesis and Photoluminescence of P-type Semiconductor Cr_2O_3 Nanowires, *Appl. Phys. Lett.,* **2006**, *88*, 241112.
(33) Choi, S.-Y.; Kim, M.-H.; Kwon, Y.-U., Effects of Cr_2O_3 Modification on the Performance of SnO_2 Electrodes in DSSCs, *Phys. Chem. Chem. Phys.,* **2012**, *14*, 3576-3582.
(34) Holt, A.; Kofstad, P., Electrical Conductivity and Defect Structure of Mg-doped Cr_2O_3, *Solid State Ionics,* **1997**, *100*, 201-209.
(35) Park, J. S.; Kim, H. G., Electrical Conductivity and Defect Models of MgO-Doped Cr_2O_3, *J. Am. Ceram. Soc.,* **1988**, *71*, 173-176.
(36) Farrell, L.; Fleischer, K.; Caffrey, D.; Mullarkey, D.; Norton, E.; Shvets, I. V., Conducting Mechanism in the Epitaxial P-type Transparent Conducting Oxide Cr_2O_3: Mg, *Phys. Rev. B,* **2015**, *91*, 125202.
(37) Ayub, I.; Berry, F. J.; Johnson, C.; Johnson, D. A.; Moore, E. A.; Ren, X.; Widatallah, H. M., Tin-, Titanium-, and Magnesium-doped α-Cr_2O_3 : Characterisation and Rationalisation of the Structures, *Solid State Commun.,* **2002**, *123*, 141-145.
(38) Chambers, S. A.; Williams, J. R.; Henderson, M. A.; Joly, A. G.; Varela, M.; Pennycook, S. J., Structure, Band Offsets and Photochemistry at Epitaxial α-Cr_2O_3/α-Fe_2O_3 heterojunctions, *Surf. Sci.,* **2005**, *587*, L197-L207.
(39) Uekawa, N.; Kaneko, K., Dopant Reduction in P-type Oxide Films upon Oxygen Absorption, *J. Phys. Chem.,* **1996**, *100*, 4193-4198.
(40) Arca, E.; Fleischer, K.; Shvets, I. V., Magnesium, Nitrogen Co-doped Cr_2O_3: A P-type Transparent Conducting Oxide, *Appl. Phys. Lett.,* **2011**, *99*, 111910.
(41) Arca, E.; Fleischer, K.; Krasnikov, S. A.; Shvets, I., Effect of Chemical Precursors On the Optical and Electrical Properties of P-type Transparent Conducting Cr_2O_3: (Mg,N), *J. Phys. Chem. C,* **2013**, *117*, 21901-21907.
(42) Aoife, B. K.; Elisabetta, A.; David, O. S.; Igor, V. S.; Graeme, W. W., Assessing the Potential of Mg-doped Cr_2O_3 as a Novel P-type Transparent Conducting Oxide, *J. Phys.: Condens. Matter,* **2016**, *28*, 125501.
(43) Pan, J.; Waghmare, U. V.; Kumar, N.; Ehi-Eromosele, C. O.; Rao, C. N. R., Effect of Nitrogen and Fluorine Co-substitution on the Structure and Magnetic Properties of Cr_2O_3, *ChemPhysChem,* **2015**, *16*, 1502-1508.
(44) Goel, S.; Kumar, A.; Quamara, J. K.; Kumar, J., Structural, Optical and Magnetic Properties of Fe Doped Cr_2O_3 Nanoparticles, *Adv. Sci. Lett,* **2014**, *20*, 1562-1566.
(45) Hagel, W. C., Anion Diffusion in α-Cr_2O_3, *J. Am. Ceram. Soc.,* **1965**, *48*, 70-75.
(46) Sabioni, A. C. S.; Lesage, B.; Huntz, A. M.; Pivin, J. C.; Monty, C., Self-diffusion in Cr_2O_3 I. Chromium Diffusion in Single Crystals, *Philos. Mag. A,* **1992**, *66*, 333-350.
(47) Sabioni, A. C. S.; Huntz, A. M.; Millot, F.; Monty, C., Self-diffusion in Cr_2O_3 II. Oxygen Diffusion in Single Crystals, *Philos. Mag. A,* **1992**, *66*, 351-360.
(48) Sabioni, A. C. S.; Huntz, A. M.; Millot, F.; Monty, C., Self-diffusion in Cr_2O_3 III. Chromium and Oxygen Grain-boundary Diffusion in Polycrystals, *Philos. Mag. A,* **1992**, *66*, 361-374.

(49) Anna, I.; Michael, N., Charge Compensation in Trivalent Cation Doped Bulk Rutile TiO_2, *J. Phys.: Condens. Matter,* **2011**, *23*, 334207.
(50) Iwaszuk, A.; Nolan, M., Electronic Structure and Reactivity of Ce-and Zr-Doped TiO_2: Assessing the Reliability of Density Functional Theory Approaches, *J. Phys. Chem. C,* **2011**, *115*, 12995-13007.
(51) Nolan, M., Enhanced Oxygen Vacancy Formation in Ceria (111) and (110) surfaces Doped with Divalent Cations, *J. Mater. Chem.,* **2011**, *21*, 9160-9168.
(52) Nolan, M., Charge Compensation and Ce^{3+} Formation in Trivalent Doping of the CeO_2 (110) Surface: The Key Role of Dopant Ionic Radius, *J. Phys. Chem. C,* **2011**, *115*, 6671-6681.
(53) Huang, R. F.; Agarwal, A. K.; Anderson, H. U., Oxygen Activity Dependence of the Electrical Conductivity of Li-Doped Cr_2O_3, *J. Am. Ceram. Soc.,* **1984**, *67*, 146-150.
(54) Hagel, W. C., Electrical Conductivity of Li-Substituted Cr_2O_3, *J. Appl. Phys.,* **1965**, *36*, 2586-2587.
(55) Carey, J. J.; Nolan, M., Cation Doping Size Effect for Methane Activation on Alkaline Earth Metal Doping of the CeO_2 (111) Surface, *Catal. Sci. Tech.,* **2016**, *6*, 3544-3558.
(56) Carey, J. J.; Nolan, M., Dissociative Adsorption of Methane on the Cu and Zn Doped (111) Surface of CeO_2, *Appl. Catal., B,* **2016**, *197*, 324-336.
(57) Heyd, J.; Scuseria, G. E., Efficient Hybrid Density Functional Calculations in Solids: Assessment of the Heyd–Scuseria–Ernzerhof Screened Coulomb Hybrid Functional, *J. Chem. Phys.,* **2004**, *121*, 1187-1192.
(58) Keating, P. R.; Scanlon, D. O.; Watson, G. W., Computational Testing of Trivalent Dopants in CeO_2 for Improved High-κ Dielectric Behaviour, *J. Mater. Chem. C,* **2013**, *1*, 1093-1098.
(59) Keating, P. R.; Scanlon, D. O.; Watson, G. W., The Nature of Oxygen States on the Surfaces of CeO_2 and La-doped CeO_2, *Chem. Phys. Lett.,* **2014**, *608*, 239-243.
(60) Kresse, G., Comput. Matter Sci. 6, 15 (1996);(d) Kresse, G., and Furthmuller, *Phys. Rev. B,* **1996**, *54*, 11,169.
(61) Kresse, G.; Furthmüller, J., Software VASP, Vienna (1999), *Phys. Rev. B,* **1996**, *54*, 169.
(62) Kresse, G.; Furthmüller, J., Efficiency of Ab-initio Total Energy Calculations for Metals and Semiconductors using a Plane-wave Basis Set, *Comp. Mater. Sci.,* **1996**, *6*, 15-50.
(63) Perdew, J. P.; Yue, W., Accurate and Simple Density Functional for the Electronic Exchange Energy: Generalized Gradient Approximation, *Phys. Rev. B,* **1986**, *33*, 8800.
(64) Perdew, J. P.; Burke, K.; Ernzerhof, M., Generalized Gradient Approximation Made Simple, *Phys. Rev. Lett.,* **1996**, *77*, 3865.
(65) Kresse, G.; Furthmüller, J., Efficient Iterative Schemes for Ab-initio Total-energy Calculations using a Plane-wave Basis Set, *Phys. Rev. B,* **1996**, *54*, 11169.
(66) Kresse, G.; Joubert, D., From Ultrasoft Pseudopotentials to the Projector Augmented-wave Method, *Phys. Rev. B,* **1999**, *59*, 1758.
(67) Monkhorst, H. J.; Pack, J. D., Special Points for Brillouin-zone Integrations, *Phys. Rev. B,* **1976**, *13*, 5188.
(68) Murnaghan, F., The Compressibility of Media Under Extreme Pressures, *P. Natl. Acad. Sci. USA,* **1944**, *30*, 244.
(69) Di Cerbo, R. K.; Seybolt, A. U., Lattice Parameters of the α-Fe_2O_3-Cr_2O_3 Solid Solution, *J. Am. Ceram. Soc.,* **1959**, *42*, 430-431.
(70) Liechtenstein, A. I.; Anisimov, V. I.; Zaanen, J., Density-functional Theory and Strong Interactions: Orbital Ordering in Mott-Hubbard Insulators, *Phys. Rev. B,* **1995**, *52*, R5467-R5470.
(71) Dudarev, S.; Botton, G.; Savrasov, S.; Humphreys, C.; Sutton, A., Electron-Energy-Loss Spectra and the Structural Stability of Nickel Oxide: An LSDA+U study, *Phys. Rev. B,* **1998**, *57*, 1505.
(72) Dudarev, S. L.; Liechtenstein, A. I.; Castell, M. R.; Briggs, G. A. D.; Sutton, A. P., Surface States on NiO (100) and the Origin of the Contrast Reversal in Atomically Resolved Scanning Tunneling Microscope Images, *Phys. Rev. B,* **1997**, *56*, 4900-4908.

(73) Bengone, O.; Alouani, M.; Blöchl, P.; Hugel, J., Implementation of the Projector Augmented-Wave LDA+U Method: Application to the Electronic Structure of NiO, *Phys. Rev. B,* **2000**, *62*, 16392-16401.

(74) Rohrbach, A.; Hafner, J.; Kresse, G., Electronic Correlation Effects in Transition-metal Sulfides, *J. Phys.: Condens. Matter,* **2003**, *15*, 979.

(75) Keating, P. R.; Scanlon, D. O.; Morgan, B. J.; Galea, N. M.; Watson, G. W., Analysis of Intrinsic Defects in CeO_2 using a Koopmans-like GGA+U Approach, *J. Phys. Chem. C,* **2012**, *116*, 2443-2452.

(76) Pisarev, R. V.; Krichevtsov, B. B.; Pavlov, V. V., Optical Study of the Antiferromagnetic-paramagnetic Phase Transition in Chromium Oxide Cr_2O_3, *Phase Transit.,* **1991**, *37*, 63-72.

(77) Uozumi, T.; Okada, K.; Kotani, A., Theory of Photoemission Spectra for M_2O_3 (M= Ti, V, Cr, Mn, Fe) Compounds, *J. Electron. Spectrosc. Relat. Phenom.,* **1996**, *78*, 103-106.

(78) Kehoe, A. B.; Scanlon, D. O.; Watson, G. W., Role of Lattice Distortions in the Oxygen Storage Capacity of Divalently Doped CeO_2, *Chem. Mater.,* **2011**, *23*, 4464-4468.

(79) Ling, L.; Song, J.; Zhao, S.; Zhang, R.; Wang, B., DFT Study on the Effects of Defect and Metal-doping on the Decomposition of H_2S on the Fe_2O_3(0001) surface, *RSC Adv.,* **2014**, *4*, 22411-22418.

(80) Abou-Ghantous, M.; Jaussaud, P. C.; Bates, C. A.; Fletcher, J. R., Further Studies of the Ni^{3+} :Al_2O_3 Jahn-Teller System, *J. Phys. C Solid State,* **1975**, *8*, 3641-3652.

(81) Abou-Ghantous, M.; Bates, C. A.; Clark, I. A.; Fletcher, J. R.; Jaussaud, P. C.; Moore, W. S., A Study of a Jahn-Teller Orbital Doublet: Ni^{3+} in Al_2O_3, *J. Phys. C Solid State,* **1974**, *7*, 2707-2720.

(82) Salce, B.; Goer, A. M. d., Studies of the Ni^{3+} :Al_2O_3 System by Thermal Conductivity Measurements, *J. Phys. C Solid State,* **1979**, *12*, 2081.

(83) Ivanova, T. A.; Petrashen', V. E.; Chezhina, N. V.; Yablokov, Y. V., Jahn-Teller Effect in Low-spin Ni^{3+} in the $LaAlO_3$ ceramic, *Phys. Solid State*, *44*, 1468-1470.

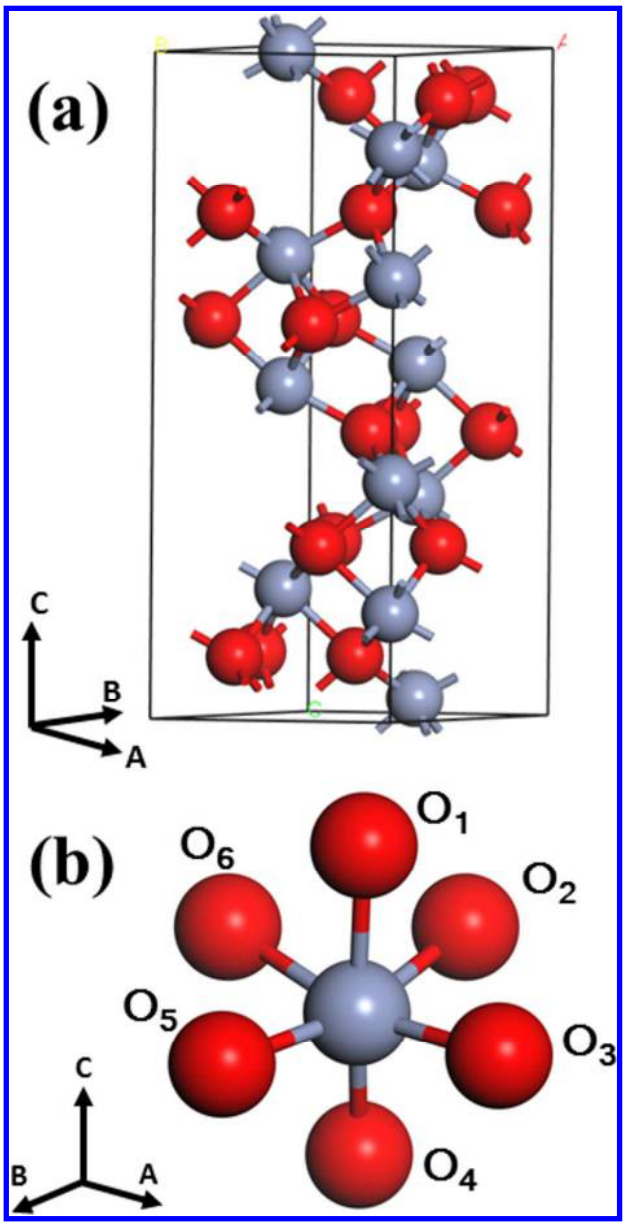

Figure 1: The atomic structure (a) and local cation geometry (b), for bulk α-Cr2O3. The blue and red spheres represent the lattice positions for Cr and O respectively. The orientation along the a-, b- and c-vectors is included to show the relative position of the cation geometry to the bulk unit cell.
Figure 1
175x347mm (300 x 300 DPI)

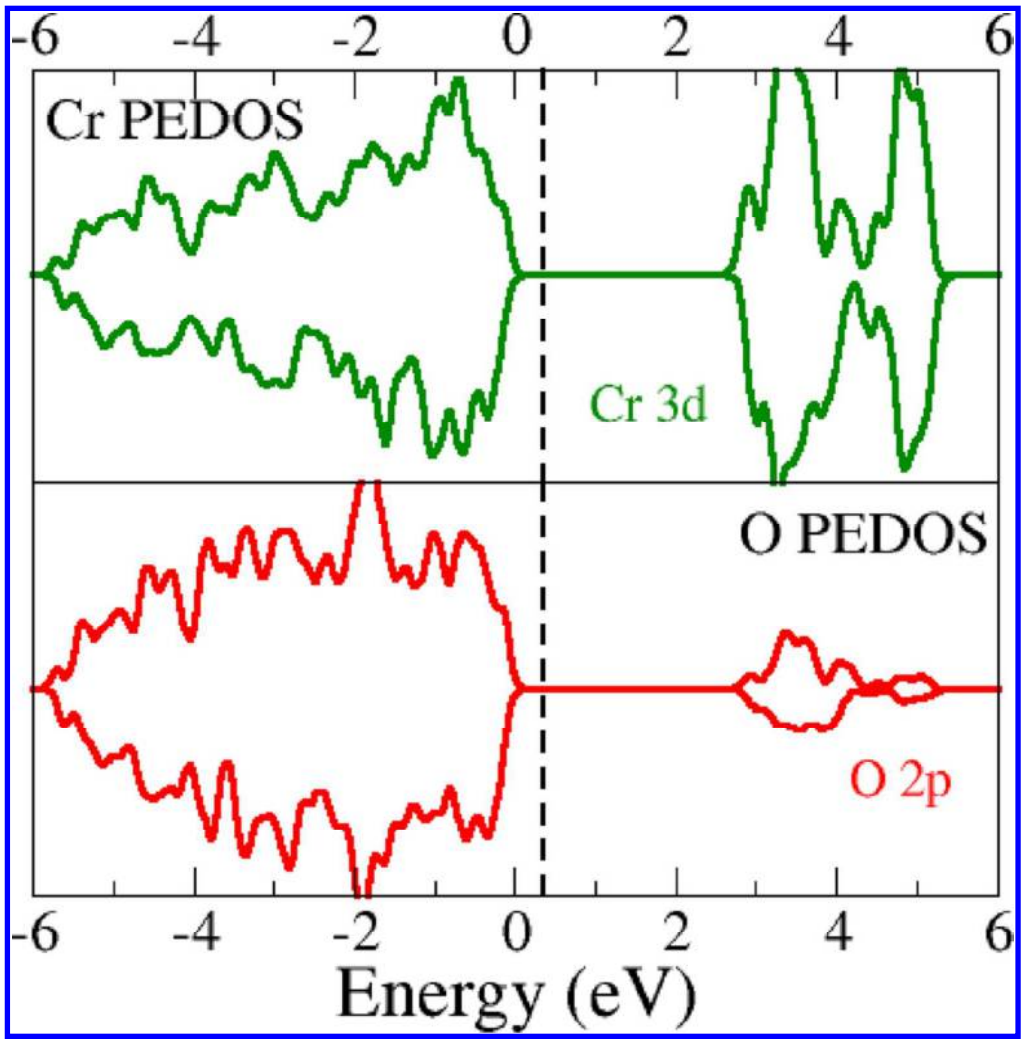

Figure 2: The calculated spin polarised PEDOS for bulk α-Cr2O3. The green and red lines are the Cr 3d and O 2p states, respectively. The top of the valence band is aligned to 0 eV and the dotted line indicates the calculated position of the Fermi Level.
Figure 2
84x85mm (300 x 300 DPI)

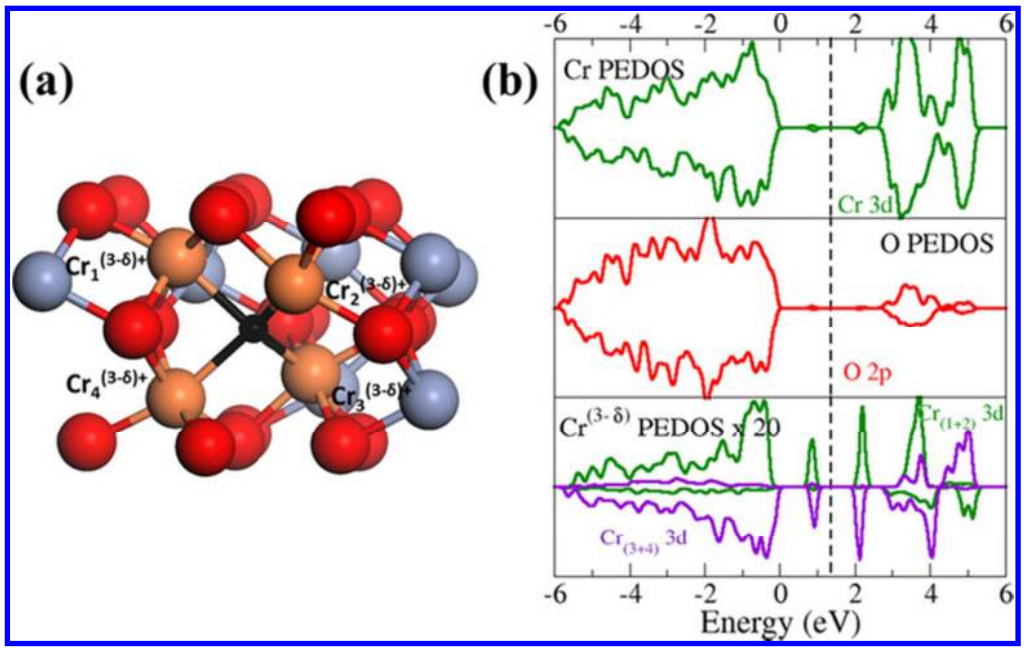

Figure 3: (a) The local atomic structure around the oxygen vacancy (indicated by a small black sphere) in bulk α-Cr2O3. The color coding is the same as figure 1 and the partially reduced Cr3+ cations are indi-cated by the orange spheres. (b) The calculated PEDOS for the reduced Cr2O3 bulk with the defect levels shown within the band gap. The top of the valence band is aligned to 0eV and the dotted line indicates the highest occupied state.

Figure 3
54x34mm (300 x 300 DPI)

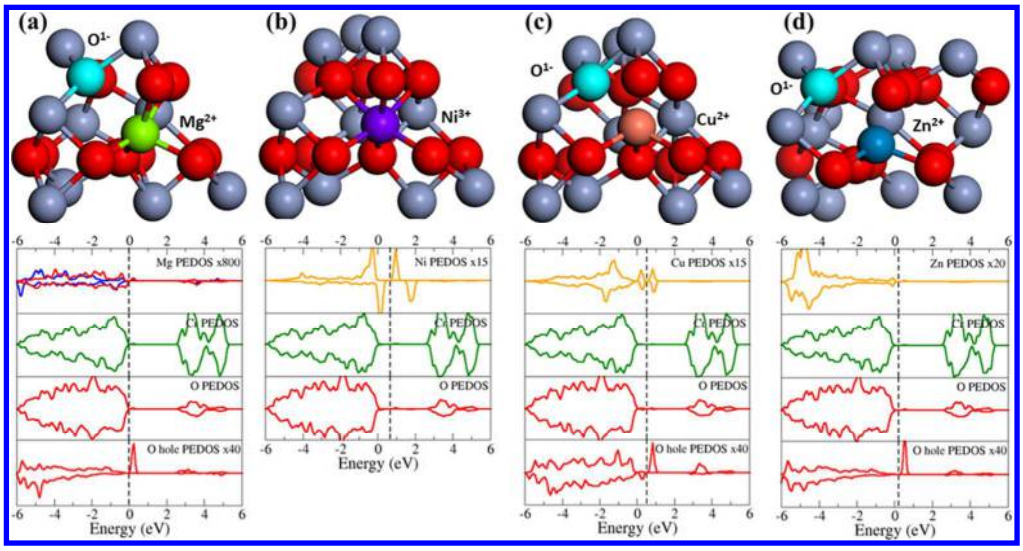

Figure 4: The local geometry and calculated PEDOS for (a) Mg, (b) Ni, (c) Cu, and (d) Ni doped α-Cr2O3. The grey and red spheres are the Cr3+ cations and O2- anions, respectively, while the Mg, Ni, Cu and Zn dopants are the green, purple, orange and blues spheres. The blue, red, orange and green lines on the PEDOS plots are the s, p, dopant 3d and Cr 3d states with the top of the valence band aligned to 0eV and the dotted line shows the position of the Fermi level.

Figure 4
86x45mm (300 x 300 DPI)

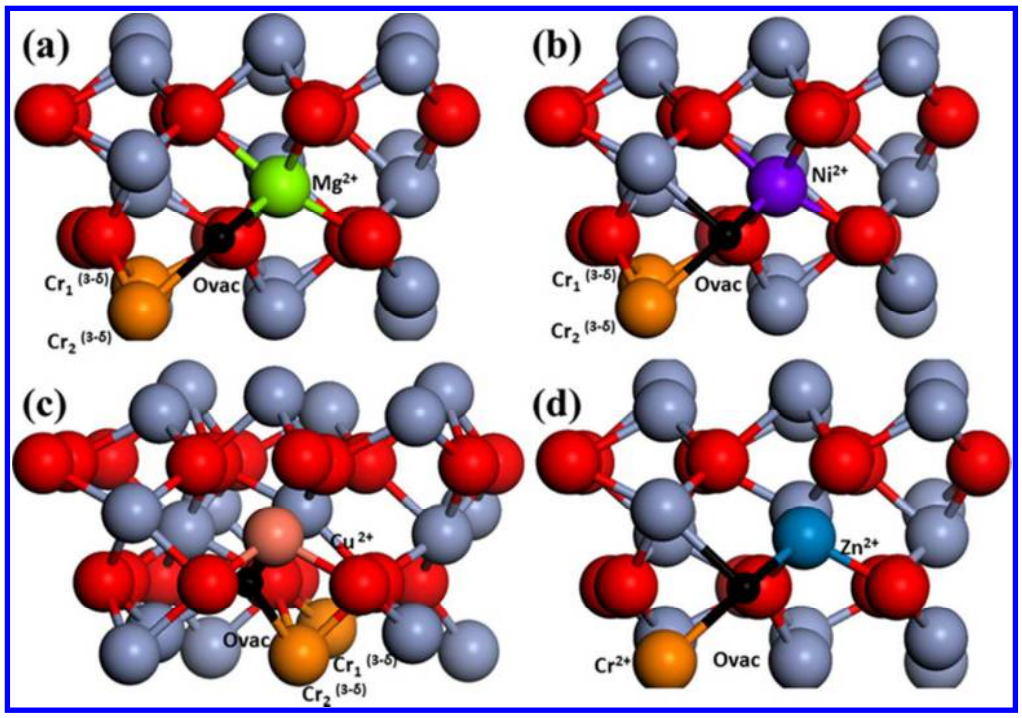

Figure 5: The calculated local geometry after formation of oxygen vacancies in (a) Mg, (b) Ni, (c) Cu and (d) Zn doped Cr2O3. The location of the oxygen vacancy is indicated by the small black sphere, while the partially reduced Cr cations are shown by the orange spheres. The green, purple, brown, and blue spheres show the location of the Mg, Ni, Cu and Zn dopants, respectively, while the lattice posi-tions of the Cr cation and O anions are shown by the grey and red spheres.

Figure 5
57x39mm (300 x 300 DPI)

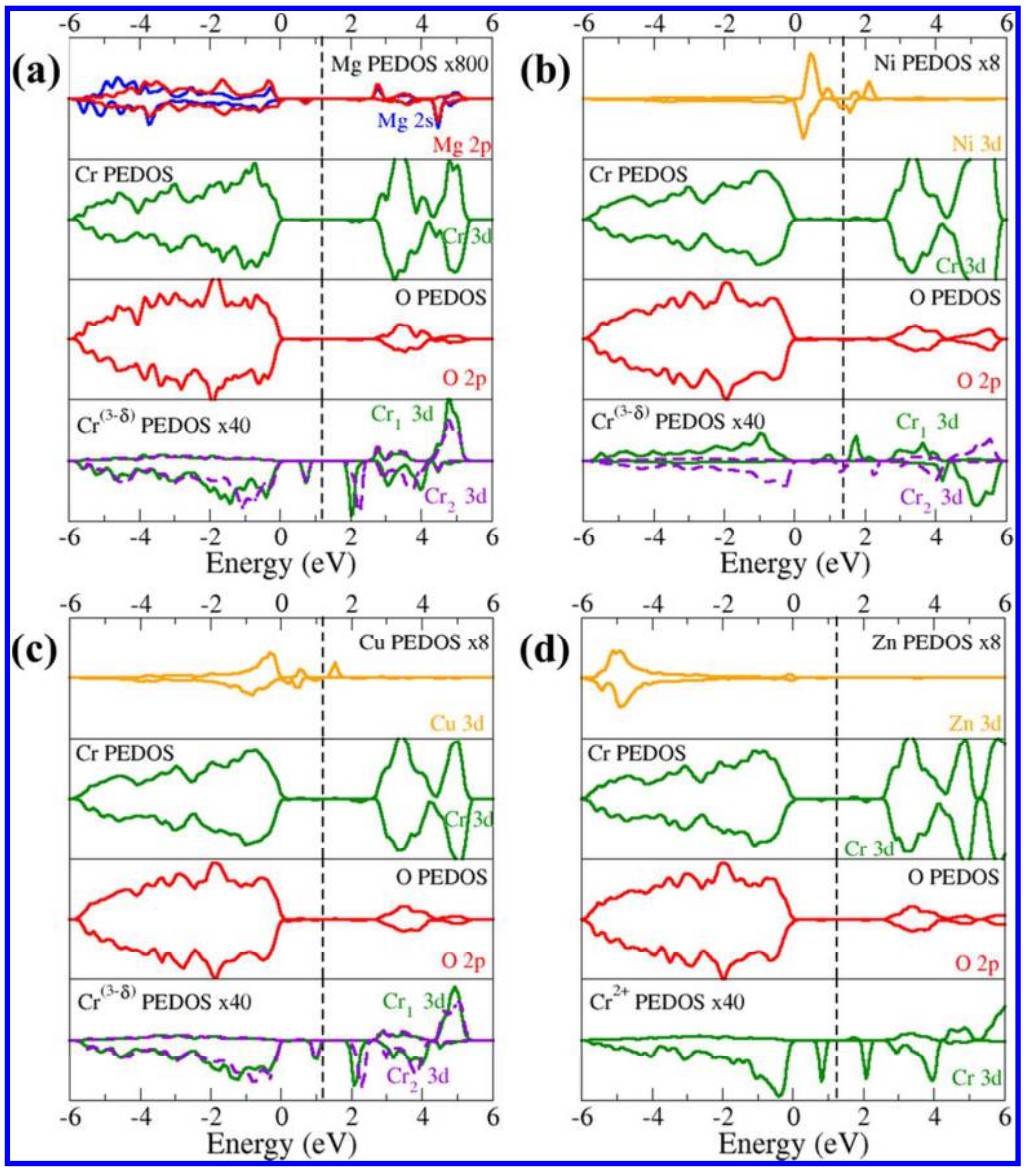

Figure 6: The calculated PEDOS plots for (a) Mg, (b) Ni, (c) Cu and (d) Zn doped Cr2O3. The green and red lines show the Cr 3d and O 2p states, while the orange lines show the Ni, Cu and Zn 3d states. The blue and red lines for Mg-Cr2O3 show the Mg 2s and 2p states respectively. The bottom panel in each case shows the PEDOS for the reduced Cr cations with the dashed purple lines show the contribution of the different coordinated Cr cation. The top of the VB in each plot is aligned to 0eV and the dashed black line shows the location of the Fermi level.

Figure 6
96x109mm (300 x 300 DPI)

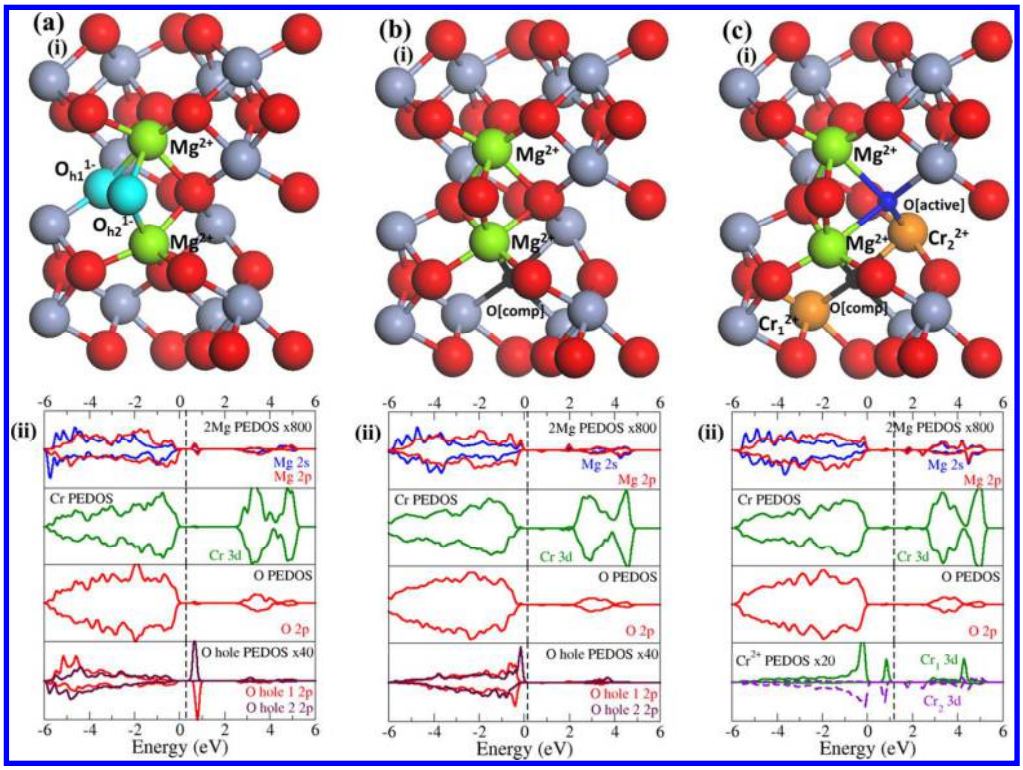

Figure 7: The local atomic structure and calculated PEDOS plots of 2Mg doped Cr2O3 for (a) two Mg dopants, (b) charge compensated structure, and (c) active oxygen vacancy. The green, grey, red, light blue and orange spheres show the lattice positions of the Mg dopant, Cr cation, O anion, O atom with hole, and reduced Cr cations respectively. The small black and blue sphere shows the location of the compensated and active oxygen vacancies. For the PEDOS plots, the blue, red and green lines show the s, p and d state contributions to the VB and CB. The top of the VB is aligned to 0eV, and the dashed black line shows the position of the Fermi level.

Figure 7
119x89mm (300 x 300 DPI)

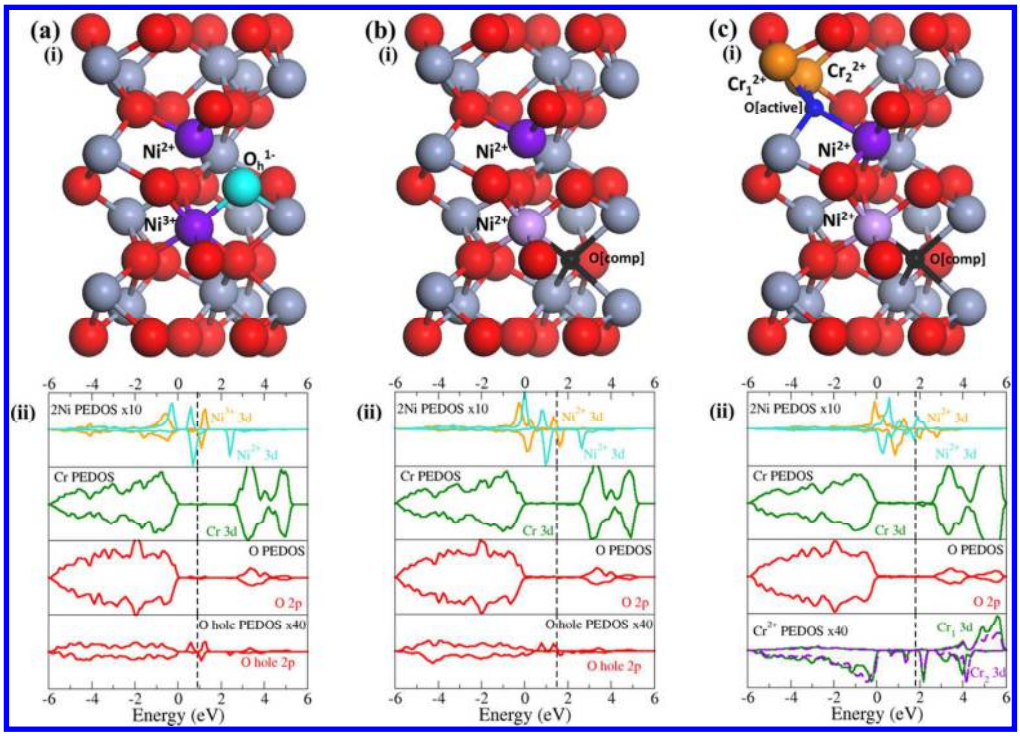

Figure 8: The local atomic structure and calculated PEDOS for 2Ni doped Cr2O3 for (a) two Ni dopants, (b) charge compensated structure, and (c) active oxygen vacancy. The purple, grey, red, light blue and orange spheres show the lattice positions of the Ni dopant, Cr cation, O anion, O atom with hole, and reduced Cr cations respectively. The small black and blue sphere shows the location of the compensated and active oxygen vacancies. For the PEDOS plots, green and red lines show the Cr 3d and O 2p state contributions to the VB and CB, while the light blue, orange lines show the contributions of the different Ni 3d states. The top of the VB is aligned to 0eV, and the dashed black line shows the position of the Fermi level.

Figure 8
116x83mm (300 x 300 DPI)

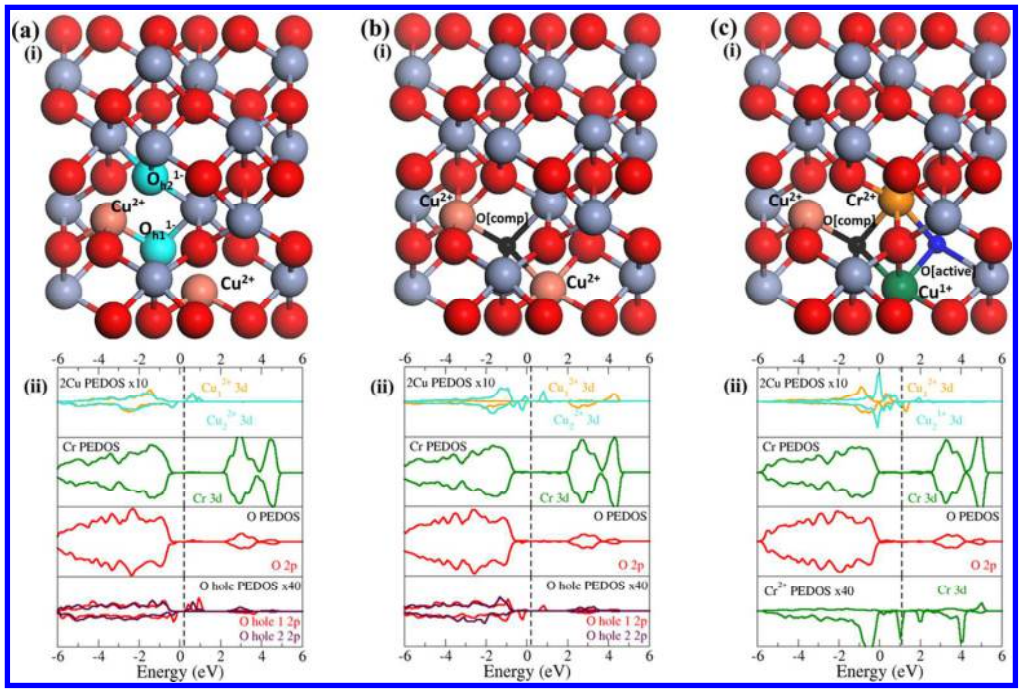

Figure 9: The local atomic structure and calculated PEDOS for 2Cu doped Cr2O3 for (a) two Cu do-pants, (b) charge compensated structure, and (c) active oxygen vacancy. The brown, grey, red, light blue and orange spheres show the lattice positions of the Cu dopant, Cr cation, O anion, O atom with hole, and reduced Cr cations respectively. The small black and blue sphere shows the location of the compen-sated and active oxygen vacancies. For the PEDOS plots, green and red lines show the Cr 3d and O 2p state contributions to the VB and CB, while the light blue, orange lines show the contributions of the different Cu 3d states. The top of the VB is aligned to 0eV, and the dashed black line shows the position of the Fermi level.

Figure 9
107x71mm (300 x 300 DPI)

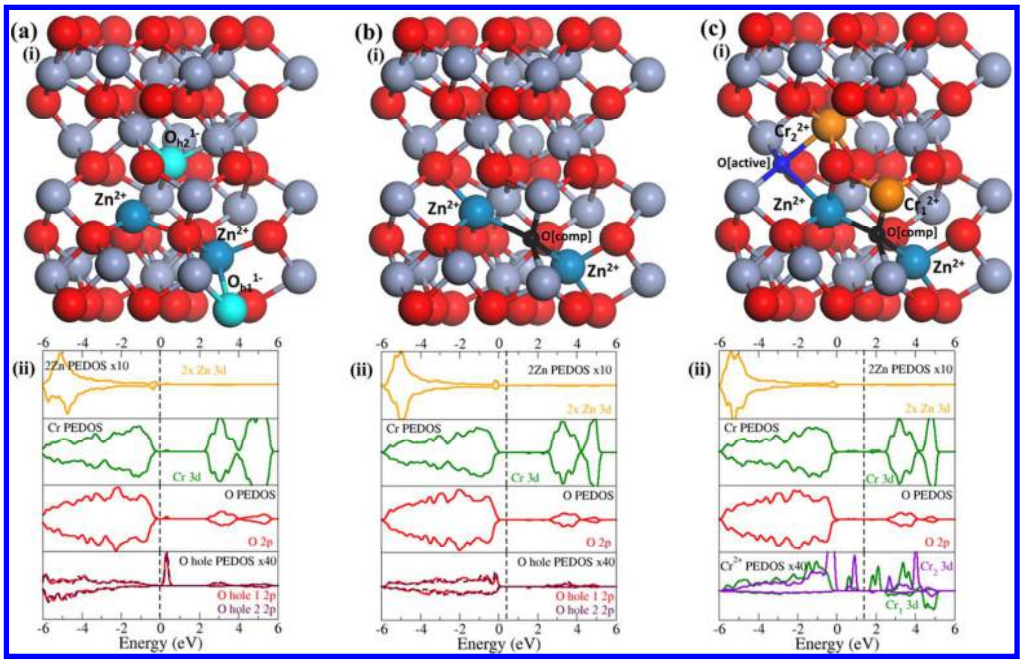

Figure 10: The local atomic structure and calculated PEDOS for 2Zn doped Cr2O3 for (a) two Zn do-pants, (b) charge compensated structure, and (c) active oxygen vacancy. The dark blue, grey, red, light blue and orange spheres show the lattice positions of the Zn dopant, Cr cation, O anion, O atom with hole, and reduced Cr cations respectively. The small black and blue sphere shows the location of the compensated and active oxygen vacancies. For the PEDOS plots, orange, green and red lines show the Zn 3d, Cr 3d and O 2p state contributions to the VB and CB, while the green and purple lines show the contributions of the different Cr2+ 3d states. The top of the VB is aligned to 0eV, and the dashed black line shows the position of the Fermi level.

Figure 10
105x67mm (300 x 300 DPI)

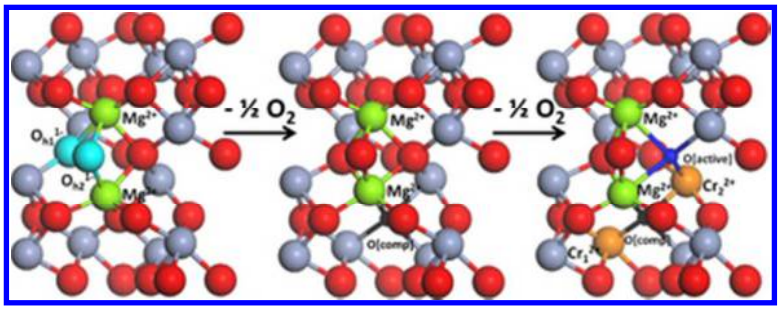

Table of contents figure
Table of contents figure
32x12mm (300 x 300 DPI)